Geochemical Perspectives Letters

A revised carbon isotope composition of the convecting upper mantle

J. Shea[1*], J. Maclennan[1], M. Edmonds[1], E. Hughes[2], M. Hartley[3], S. Mikhail[4], M. Perfit[5], O. Shorttle[1,6*]

OPEN ACCESS

https://doi.org/10.7185/geochemlet.2610

Abstract

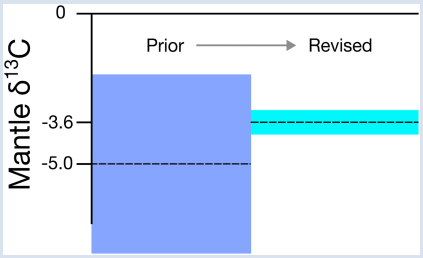

The carbon isotope composition of the convecting upper mantle is key to constraining Earth's carbon budget. Canonical estimates place upper mantle $\delta^{13}C$ between −4 and −6 ‰, but recent measurements suggest inter-ocean basin heterogeneity of several per mille. We test this hypothesis using high precision secondary ion mass spectrometry on olivine hosted melt inclusions from two contrasting settings: mid-ocean ridge basalts from the East Pacific Rise and plume influenced basalts from Iceland's Northern Volcanic Zone. Both melt inclusion suites yield indistinguishable $\delta^{13}C$ compositions despite sampling the upper mantle in different tectonic environments. We propose the convecting upper mantle $\delta^{13}C = -3.6 \pm 0.2$ ‰ (95 % confidence interval; CI), with source heterogeneity present at ±0.8 ‰ (1σ). Use of this new $\delta^{13}C$ value changes the global carbon mass balance and yields a fractional organic carbon burial of $13.7^{+2.3}_{-2.1}$ % (68 % CI), resolving previous discrepancies between isotopic and sedimentary inventory based estimates. Our results have implications for the deep carbon cycle, reducing the need to invoke large carbonate contributions to arc emissions and refining estimates of recycled organic carbon in mantle-derived reservoirs such as diamonds, carbonatites and kimberlites.

Received 21 October 2025 | Accepted 24 February 2026 | Published 7 April 2026

Introduction

The carbon isotope ($\delta^{13}C$) composition of the convecting upper mantle underpins models of core formation, volatile cycles, and bulk silicate Earth (BSE) composition, with implications for carbon budgets and climate (Kump and Arthur, 1999; Wood *et al.*, 2013; Horita and Polyakov, 2015). These calculations rely on indirect proxies sampling distinct mantle reservoirs: peridotitic diamonds (−4.9 ± 1.9 ‰; Stachel *et al.*, 2022) are a metasomatic phase (Cartigny *et al.*, 2014); mantle xenoliths (−5 ‰; Deines, 2002) reflect the lithospheric, not convecting, mantle; and carbonatites (−4.2 ± 2.1 ‰; Moussallam, 2025) record localised heterogeneities rather than typical upper mantle compositions. Direct measurements from un-degassed MORB glasses, such as Mid-Atlantic Ridge (MAR) *'popping rocks'* (~−4 ‰; Javoy and Pineau, 1991; Pineau *et al.*, 2004; Bekaert *et al.*, 2024), provide valuable constraints but depend on accurate accounting for CO_2-rich bubble accumulation, which can decouple bulk carbon isotope compositions from the original melt.

Recent advances in secondary ion mass spectrometry (SIMS) now enable routine $\delta^{13}C$ measurement of olivine hosted melt inclusions, providing direct access to mantle carbon isotope compositions (Lee *et al.*, 2024a; Shea *et al.*, 2025). These inclusions better preserve pre-degassed $\delta^{13}C$ than low pressure quenched glasses, where equilibrium degassing enriches residual melts in ^{12}C as ^{13}C partitions into the vapour phase (Javoy *et al.*, 1978; Mattey *et al.*, 1990; Lee *et al.*, 2024b). Initial applications to natural samples challenge the notion of a homogenous mantle $\delta^{13}C$. Moussallam *et al.* (2025b) reported Pacific upper mantle values ($\delta^{13}C = -8.4 \pm 1.1$ ‰, 1σ) markedly lower than Atlantic values (−3.9 ± 0.4 ‰, 1σ), yet consistent with Southwest Indian Ridge measurements (−7.5 ± 1.4 ‰, 2 s.e.; Moussallam *et al.*, 2025a). Fagradalsfjall melt inclusions (−6.5 ± 2.5 ‰) likewise suggest heterogenous mantle carbon, with local variation (−4 and −9 ‰) implying organic carbon contributions in the Iceland plume (Moussallam *et al.*, 2024). These measurements indicate significant mantle heterogeneity and an average $\delta^{13}C$ lower than the canonical −5 ‰ (Deines, 2002; Stachel *et al.*, 2022).

Previous work has argued that large inter-basin $\delta^{13}C$ heterogeneity may reflect mantle structure, with Pacific subduction zones introducing isotopically light recycled carbon, Atlantic ridges sampling less contaminated mantle, and the Iceland plume carrying variable organic inputs. However, these interpretations rest on small sample data sets (five inclusions for a single location; Moussallam *et al.*, 2025b), and limited CO_2

1. Department of Earth Sciences, University of Cambridge, Cambridge, CB2 3EQ, UK
2. Department of Earth Sciences, University College London, London, WC1E 6BS, UK
3. Department of Earth and Environmental Sciences, University of Manchester, Manchester, M13 9PL, UK
4. School of Earth and Environmental Sciences, University of St Andrews, St Andrews, KY19 9TS, UK
5. Department of Geological Sciences, University of Florida, Gainesville, FL 32611, USA
6. Institute of Astronomy, University of Cambridge, Cambridge, CB3 0HA, UK
* Corresponding authors (emails: jjs83@cam.ac.uk; os258@cam.ac.uk)

concentrations (<250 μg g^{-1} CO_2; Moussallam *et al.*, 2025b). One concern is that this previous work may have captured degassing related fractionation rather than primary mantle $\delta^{13}C$.

We test the null hypothesis that the convecting upper mantle is homogeneous in carbon isotope composition. Using the SIMS protocol of Shea *et al.* (2025), we obtained 85 $\delta^{13}C$ measurements on melt inclusions ($n = 73$), embayments ($n = 6$) and matrix glasses ($n = 6$) from the Siqueiros Transform Fault (East Pacific Rise, EPR) and Borgarhraun (Iceland). Siqueiros represents the primitive end member of the EPR D-MORB (depleted), with minimal fractionation or mixing, whereas Borgarhraun tephra reflect primitive melts from the North Atlantic spreading ridge influenced by the Iceland plume. Their un-degassed melt inclusions define the canonical CO_2/Ba ratio of 100 ± 50 for the convecting mantle (Le Voyer *et al.*, 2017; Hauri *et al.*, 2018; Hirschmann, 2018), underpinning global estimates of mantle carbon content and surface flux *via* melting and degassing (Pacific: Saal *et al.*, 2002; Atlantic: Hauri *et al.*, 2018). Together, these sites can be used to test the Pacific-Atlantic dichotomy in ridge and plume settings. Our samples span 6.38–1678 μg g^{-1} CO_2 and include both mantle-like and degassed CO_2/Ba ratios, allowing independent recognition of degassing modification. We compare melt inclusion results to erupted MORB glass measurements from both the EPR and MAR. Analytical and modelling details are provided in the Supplementary Information.

Results and Discussion

Testing for carbon degassing. CO_2-Ba systematics (Fig. 1) show that despite contrasting petrogenetic histories, which do not bias $\delta^{13}C$ (see SI), Borgarhraun and Siqueiros melt inclusions preserve near-primary volatile compositions, making them ideal for constraining upper mantle $\delta^{13}C$. Inclusions and embayments from both locations have CO_2 concentrations of 36.3–1678 μg g^{-1} and plot along the mantle reference trend (CO_2/Ba = 100 ± 50), indicating minimal pre-entrapment degassing. Carbon undersaturated MORB glasses overlap this trend, confirming it as characteristic of un-degassed spreading ridge melts (Le Voyer *et al.*, 2017; Hirschmann, 2018; Hauri *et al.*, 2018). Most carbon saturated MORB and Icelandic glasses fall to lower CO_2/Ba, reflecting degassing.

Melt inclusion CO_2 concentrations decrease systematically toward matrix glasses (Fig. 2), reflecting progressive volatile loss during ascent and eruption. Borgarhraun matrix glasses show extensive degassing (<10 μg g^{-1} CO_2), typical of subaerial Icelandic lavas (Barry *et al.*, 2014). The most degassed glasses, from Borgarhraun, record the most negative $\delta^{13}C$ values observed in basalts, indicating extreme isotopic fractionation of >99.9 % CO_2 loss (Fig. 2). In contrast, submarine Siqueiros matrix glasses overlap with melt inclusion compositions (Saal *et al.*, 2002), showing they retained volatiles upon eruption. The agreement between melt inclusions and primary CO_2/Ba ratios confirms that our $\delta^{13}C$ data represent upper mantle, not degassing-modified, compositions.

We screened all samples for degassing using statistical outliers and degassing models to ensure $\delta^{13}C$ measurements reflect primary compositions. Weighted mean $\delta^{13}C$ from all melt inclusions embayment at both sites is −3.7 ± 1.6 ‰ (1σ), representing an initial estimate of mantle $\delta^{13}C$. Samples with *z*-scores >3 s.d. were flagged as degassed (red diamonds in Fig. 2). This identified two Borgarhraun and one Siqueiros outlier (<5 % of total data set). Their $\delta^{13}C$ values (range: −7.56 to −8.50 ‰) are systematically lower and contain intermediate CO_2 concentrations that align with partial open system equilibrium degassing trajectories (Fig. 2), confirming partial carbon loss; these were excluded. Siqueiros matrix glasses and Borgarhraun embayments show $\delta^{13}C$-CO_2 consistent with melt inclusions, representing the final pre-eruptive magma recharge, and are retained as primary values.

Carbon isotope homogeneity across ocean basins. Following filtering of degassed melt inclusions, Borgarhraun samples yield a weighted mean $\delta^{13}C = -3.52 \pm 0.12$ ‰ ($n = 47$), while Siqueiros samples yield $\delta^{13}C = -3.66 \pm 0.22$ ‰ ($n = 31$). Although these means differ by 0.14 ‰, this offset is smaller than the standard error of the difference (~0.25 ‰), indicating statistical indistinguishability. The 95 % confidence intervals (Borgarhraun, −3.76 to −3.28 ‰; Siqueiros, −4.10 to −3.22 ‰)

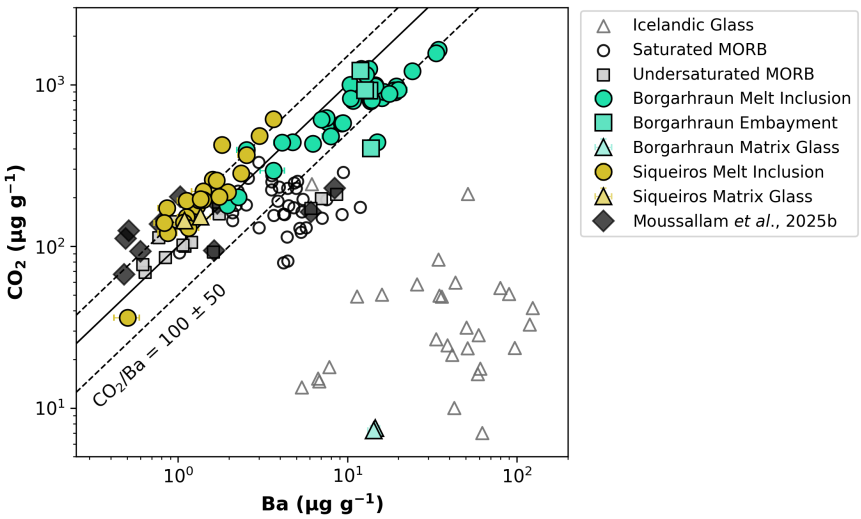

Figure 1 Test for carbon saturation using CO_2 *versus* Ba. Carbon undersaturated melts define CO_2/Ba = 100 ± 50, consistent with undersaturated mantle values prior to degassing. Borgarhraun and Siqueiros melt inclusions and embayments plot within this range, overlapping carbon undersaturated MORB, whereas carbon saturated MORB define higher CO_2/Ba. Siqueiros matrix glasses plot within mantle values; however, Borgarhraun matrix glasses show significant degassing, consistent with other Icelandic glasses that plot at lower CO_2 for a given Ba. Additional MORB glasses from Moussallam *et al.* (2025b) and Icelandic literature data (Barry *et al.*, 2014; Marshall *et al.*, 2024) are shown for comparison.

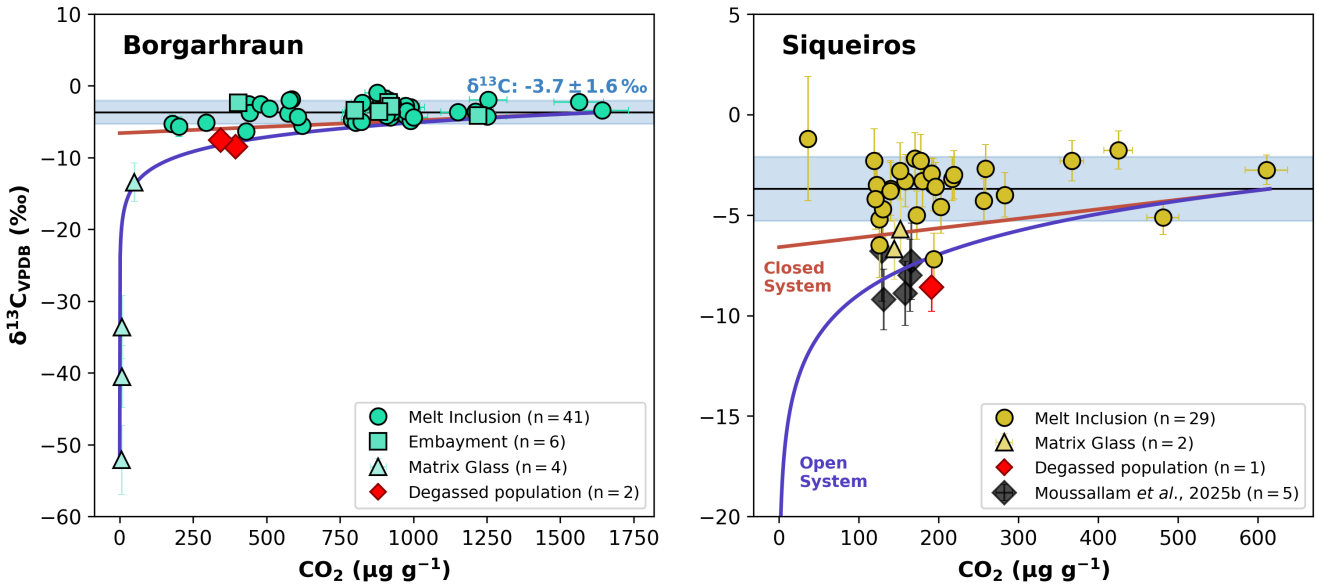

Figure 2 Testing for degassed compositions in Borgarhraun (left) and Siqueiros (right). Melt inclusions (circles), embayments (squares), and matrix glass (triangles) are shown; red diamonds indicate degassed outliers ($|z| > 3$; see SI). Closed and open system degassing curves (brown, purple) use a fractionation factor of +2.9 ‰ (Lee *et al.*, 2024a) and initial mantle $\delta^{13}C$ of −3.7 ± 1.6 ‰ (black line, blue shading), with initial CO_2 from the highest melt inclusion concentrations. Black diamonds show Siqueiros melt inclusion data from Moussallam *et al.* (2025b). Uncertainties are 1σ.

show substantial overlap, with a common range spanning 0.54 ‰. This overlap encompasses most of both uncertainty ranges, confirming that any apparent difference between the locations reflects analytical uncertainty rather than genuine source heterogeneity.

Inverse variance weighting of both data sets yields a combined constraint of $\delta^{13}C = -3.6 \pm 0.2$ ‰ (95 % CI, $n = 78$; Fig. 3; see SI for further details). This analysis yields the most precise estimate of the carbon isotopic composition of the upper mantle yet obtained. The weighting favours Borgarhraun (76 %) due to its superior individual-sample measurement precision, but both locations contribute meaningfully to the final constraint.

Mantle source heterogeneity. Un-degassed melt inclusions reveal significant over dispersion beyond analytical uncertainties: z-score standard deviations are $\sigma_z = 1.40$ (95 % CI; 1.10–1.8) for Borgarhraun, and $\sigma_z = 1.05$ (95 % CI; 0.83–1.4) for Siqueiros. Combined data yield $\sigma_z = 1.26$ (95 % CI; 1.10–1.5), indicating excess variance relative to analytical uncertainty. Over dispersion ($\sigma_z > 1$) indicates isotopic heterogeneity within mantle sources. Individual melt batches captured by melt

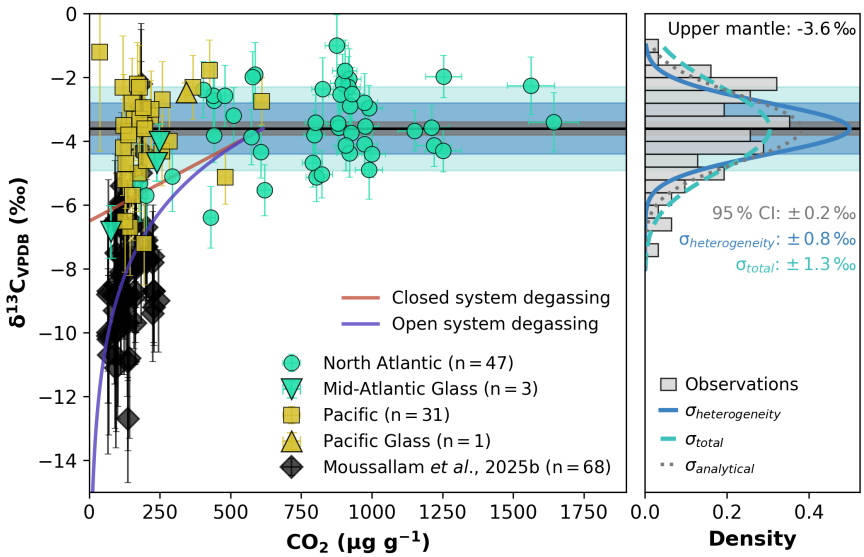

Figure 3 $\delta^{13}C$ (‰ VPDB) *versus* CO_2 (μg g^{-1}) for un-degassed, olivine hosted melt inclusions and new glass measurements from the Atlantic and Pacific compared to literature data from Moussallam *et al.* (2025b). The solid black line shows the preferred convecting upper mantle value (−3.6 ‰), with shaded bands showing the 95 % confidence interval (±0.2 ‰; grey), intrinsic mantle heterogeneity ($\sigma_{heterogeneity}$ = ± 0.8 ‰; blue), and expected observed scatter including analytical uncertainty (σ_{total} = ± 1.3 ‰; teal). Degassing curves show equilibrium closed and open system fractionation trajectories. The right panel shows the $\delta^{13}C$ distribution of un-degassed melt inclusions with Gaussian curves illustrating analytical, heterogeneity, and total variance components. Uncertainty bars are 1σ.

inclusions and embayments preserve isotopically distinct mantle signatures that are otherwise homogenised during substantial mixing in the magma chamber. Variance decomposition quantifies this natural mantle heterogeneity at 0.8 ‰ (1σ; SI). Melt inclusions sample melts that have undergone partial mixing during melt transport and storage, which reduces compositional variance. Therefore, this value likely represents a minimum estimate of intrinsic variability in the convecting mantle.

The coexistence of a consistent mean $\delta^{13}C$ with local scale heterogeneity reflects mantle convection dynamics: sufficiently vigorous for mingling of mantle sources, yet incomplete enough to preserve short length-scale isotopic variability. The upper mantle is stirred, but not mixed, by diffusive homogenisation, so preserves isotopic heterogeneity inherent to melting domains within a larger homogenous mantle that maintains long length-scale bulk compositions. We recommend $\delta^{13}C = -3.6 \pm 0.2$ ‰ (95 % CI) as the convecting upper mantle mean, with 0.8 ‰ (1σ) natural heterogeneity.

Our proposed $\delta^{13}C$ value is supported by measurements of additional MORB glasses: a Pacific glass (East Pacific Rise, ALV981-R23; Shea *et al.*, 2025) and three MAR glasses reported here (CH98-DR02, CH98-DR12 and CH98-DR17). Two MAR glasses erupted at depth (4185 and 4300 m) and overlap with the mantle heterogeneity range of our convecting upper mantle value. In contrast, a third MAR glass contains a low CO_2 (76.8 μg g^{-1} CO_2) and lower $\delta^{13}C$ (-6.8 ± 0.8 ‰), consistent with extensive equilibrium degassing associated with its shallower eruption depth (1800 m). Similarly, the MORB glass data set of Moussallam *et al.* (2025b) spans the mantle heterogeneity range at higher CO_2 concentrations but includes many samples with lower $\delta^{13}C$ and CO_2, consistent with degassing of MORB melts during ascent rather than reflecting primary mantle composition (Fig. 3).

Previously reported MORB glasses (Moussallam *et al.*, 2025a) include many degassed samples that, if treated as primary, bias mantle $\delta^{13}C$ estimates toward lower values. In contrast, our constraint (-3.6 ± 0.2 ‰) closely matches the pristine *'popping rock'* MORB glass (−3.36 ‰; Bekaert *et al.*, 2024). While indirect proxies such as peridotitic diamonds (-4.9 ± 1.9 ‰), mantle xenoliths (~−5 ‰), and carbonatites (-4.2 ± 2.1 ‰) span broad and poorly constrained ranges that partly overlap our estimate; they sample distinct mantle reservoirs rather than the convecting upper mantle accessed by spreading ridge magmatism.

Basis for broad $\delta^{13}C$ homogeneity in the convecting upper mantle. Isotopic uniformity across spreading ridges reflects efficient mantle convection operating on time scales (10^6–10^7 years; Coltice and Schmalzl, 2006) shorter than carbon's mantle residence time (>1 Gyr to ~4.6 Gyr; Dasgupta and Hirschmann, 2010), ensuring effective homogenisation of isotope heterogeneities from subduction zones. Carbon's chemical behaviour further facilitates homogenisation; it depresses the mantle solidus, has strong incompatibility, and shows high silicate melt solubility, promoting redistribution and mixing by incipient melting across large mantle volumes (Green and Wallace, 1988; Ni and Keppler, 2013; Rosenthal *et al.*, 2015). At depth, redox melting during decompression driven breakdown of carbon-bearing phases creates carbonatite melts that remain mobile even at very low melt fractions (<1 wt. %; Rohrbach and Schmidt, 2011; Minarik and Watson, 1995). This property of carbonate melts facilitates efficient isotopic equilibrium. Carbon's long residence time and its chemical behaviour promotes homogenisation of long length-scale variation in the convecting upper mantle.

Carbon cycle implications. Our constraint on the convecting upper mantle $\delta^{13}C$ (-3.6 ± 0.2 ‰) represents a ~1.3 ‰ shift toward more positive values from widely used canonical estimates of −4 to −6 ‰, with broad implications for carbon cycling between Earth's reservoirs. This heavier mantle carbon composition requires revision of BSE carbon budgets and affects global mass balance calculations, from subduction input to volcanic output fluxes, which anchor carbon atmospheric fluxes. Incorporating natural mantle heterogeneity (0.8 ‰, 1σ), a population mean primary magmatic $\delta^{13}C$ value lower than −4.4 ‰ (mean minus 1σ natural heterogeneity) likely indicates recycled contributions, shifting the threshold for recycled carbon input from −6 ‰ to −4.4 ‰.

The mean $\delta^{13}C$ of melt inclusions from mantle derived melts should scatter within the 0.8 ‰ inherent heterogeneity of the −3.6 ‰ mantle mean, providing a baseline for distinguishing primary melt compositions, potentially degassed magmas, or contributions from recycled carbon components. Using previously established -4.9 ± 1.9 ‰ mantle estimates from diamonds, 69 % of diamonds were classified as sampling solely mantle derived carbon (Cartigny *et al.*, 2014; Stachel *et al.*, 2022). Within the framework of this mass balance, our constraint suggests instead that most diamonds are consistent with contributions from ^{13}C-depleted recycled organic carbon: peridotitic diamonds (average $\delta^{13}C = -4.9 \pm 1.9$ ‰) reflect convecting mantle carbon with minor recycled contributions, whereas asthenospheric and transition zone diamonds (-9.4 ± 6.7 ‰) and lower mantle diamonds (-14.5 ± 7.2 ‰) record recycled organic carbon subducted into Earth's deep interior (Stachel *et al.*, 2022). This either reflects a strong bias in the sampling of sub-lithospheric diamonds, a more carbon-poor deep Earth, or diamond formation being internalised within deeply subducted slabs and therefore low mantle carbon contributions. Many carbonatites ($\delta^{13}C = -4.2 \pm 2.1$ ‰; Moussallam, 2025) are consistent with melting of the convecting mantle. Kimberlites and associated melts span a wide $\delta^{13}C$ (range −1.2 to −10.8 ‰, average -5.2 ± 1.2 ‰, 1σ; Giuliani *et al.*, 2025), most consistent with melting of the convecting mantle followed by degassing rather than by melting a mantle source modified by organic or crustal carbonate assimilation (Fig. S-3).

Our revised mantle $\delta^{13}C$ value enables more accurate quantification of volcanic degassing and volatile fluxes. Mason *et al.* (2017) attributed elevated volcanic arc gas $\delta^{13}C$ values (−3.8 to −4.6 ‰) in comparison to a MORB source (−6.0 ‰) to crustal carbonate assimilation. Our baseline, however, suggests these gas values fall within the range of intrinsic mantle heterogeneity, removing the requirement for widespread incorporation of ^{13}C-enriched recycled carbonate or crustal carbonate assimilation in petrogenetic models.

Global carbon cycle mass balance depends on the fraction of organic carbon buried in the solid Earth (f_{org}). We estimate f_{org} using Monte Carlo uncertainty propagation of the standard two end member carbon isotope mass balance (*e.g.*, Derry, 2014):

$$\delta^{13}C_{in} = \delta^{13}C_{org} f_{org} + \delta^{13}C_{carb}(1 - f_{org}),$$

where $\delta^{13}C_{in}$ is the mantle input composition, and $\delta^{13}C_{org}$ and $\delta^{13}C_{carb}$ are the organic and carbonate end members. Using our revised mantle value ($\delta^{13}C_{in} = -3.6 \pm 0.2$ ‰), we obtain $f_{org} = 13.7^{+2.3}_{-2.1}$ % (68 % CI; see SI). This aligns with sedimentary estimates (10–17 %; Derry, 2014) and overlaps, but is lower than, estimates derived from high temperature volcanic gas emissions (15.2 to 18.4 %; Mason *et al.*, 2017).

Previous isotope based estimates of $f_{org} = 19$–34 % assumed mantle carbon isotope compositions of −5 to −6 ‰ using an equivalent mass balance approach (Derry, 2014). Applying the same Monte Carlo framework, using an earlier

mantle value (−4.9 ± 1.9 ‰; Stachel *et al.*, 2022) reproduces similarly elevated burial fractions (Figs. S-5, S-6), demonstrating that the discrepancy arises directly from the assumed mantle isotope composition and its uncertainty. The heavier mantle value determined here resolves this inconsistency and establishes a revised baseline for global carbon cycle mass balance. A lower f_{org} reduces the requirement for long term organic carbon burial to balance mantle degassing *via* volcanism, providing tighter closure on organic burial in Earth's long term carbon cycle.

Conclusions

We establish $\delta^{13}C = -3.6 \pm 0.2$ ‰ as the convecting upper mantle carbon isotope composition, an order of magnitude improvement in precision over previous estimates. This value derives from olivine hosted melt inclusions from distinct spreading ridges: Pacific MORB (Siqueiros Transform Fault) and plume influenced North Atlantic basalts (Borgarhraun, Iceland). Statistical equivalence between these sites (−3.5 ± 0.1 ‰ and −3.7 ± 0.2 ‰), despite ~7000 km separation and contrasting geodynamic settings, indicates large scale isotopic uniformity in bulk mantle, while preserving natural source heterogeneity (0.8 ‰, 1σ) at the melt region scale. Apparent mantle $\delta^{13}C$ heterogeneity in earlier work reflects volatile loss, where CO_2-depleted samples yield systematically lower $\delta^{13}C$ values following degassing trajectories. Such degassed samples artificially bias estimates of mean mantle composition and heterogeneity.

Our revised $\delta^{13}C$ value reframes global carbon cycling. This ~1.3 ‰ shift toward more positive values relative to widely used estimates redefines the recycled carbon threshold to −4.4 ‰, indicating many peridotitic diamonds previously considered mantle derived may contain recycled organic carbon. This baseline also removes the need for substantial crustal carbonate assimilation in volcanic arc gases. Monte Carlo mass balance gives $f_{org} = 13.7^{+2.3}_{-2.1}$ % (68 % CI), consistent with sedimentary inventories (10–17 %) rather than isotopic calculations (19–34 %; Derry, 2014). This value refines end member compositions for global carbon flux models and improves constraints on natural carbon cycle baselines.

Author Contributions and Acknowledgements

JS conceived and led the study, performed SIMS analyses, developed the statistical framework, conducted Monte Carlo modelling, and wrote the manuscript. JM, OS, and ME contributed to study design, interpretation, and manuscript development. EH, MH, SM, and MP contributed to interpretation and manuscript revision. All authors contributed to discussion and approved the final manuscript. We thank Brian Monteleone for expert assistance with SIMS analyses at the Northeast National Ion Microprobe Facility at Woods Hole Oceanographic Institution, operated under the direction of Glenn Gaetani. We thank Iris Buisman for assistance with electron microprobe analyses. We thank Jason Day for assistance with LA-ICP-MS analyses, operated under the direction of Sally Gibson. JS, OS, JM, MH, and SM acknowledge support from UKRI grant NE/V011383/1. JS and OS acknowledge support from the Leverhulme Centre for Life in the Universe Joint Collaborations Research Project Grant G112026/LBAG429. We thank Raúl Fonseca for editorial handling of the manuscript, and David Bekaert and an anonymous reviewer for constructive comments that improved the manuscript.

Editor: Raul O.C. Fonseca

Additional Information

Supplementary Information accompanies this letter at https://www.geochemicalperspectivesletters.org/article2610.

Cite this letter as: Shea, J., Maclennan, J., Edmonds, M., Hughes, E., Hartley, M., Mikhail, S., Perfit, M., Shorttle, O. (2026) A revised carbon isotope composition of the convecting upper mantle. *Geochem. Persp. Let.* 39, 36–41. https://doi.org/10.7185/geochemlet.2610

References

Barry, P.H., Hilton, D.R., Füri, E., Halldórsson, S.A., Grönvold, K. (2014) Carbon isotope and abundance systematics of Icelandic geothermal gases, fluids and subglacial basalts with implications for mantle plume-related CO_2 fluxes. *Geochimica et Cosmochimica Acta* 134, 74–99. https://doi.org/10.1016/j.gca.2014.02.038

Bekaert, D.V., Barry, P.H., Curtice, J., Blusztajn, J., Hudak, M., Seltzer, A., Broadley, M.W., Krantz, J.A., Wanless, V.D., Soule, S.A., Mittelstaedt, E., Kurz, M.D. (2024) A carbon, nitrogen, and multi-isotope study of basalt glasses near 14°N on the Mid-Atlantic Ridge. Part A: Degassing processes. *Geochimica et Cosmochimica Acta* 369, 160–178. https://doi.org/10.1016/j.gca.2023.12.015

Cartigny, P., Palot, M., Thomassot, E., Harris, J.W. (2014) Diamond Formation: A Stable Isotope Perspective. *Annual Review of Earth and Planetary Sciences* 42, 699–732. https://doi.org/10.1146/annurev-earth-042711-105259

Coltice, N., Schmalzl, J. (2006) Mixing times in the mantle of the early Earth derived from 2-D and 3-D numerical simulations of convection. *Geophysical Research Letters* 33, L23304. https://doi.org/10.1029/2006GL027707

Dasgupta, R., Hirschmann, M.M. (2010) The deep carbon cycle and melting in Earth's interior. *Earth and Planetary Science Letters* 298, 1–13. https://doi.org/10.1016/j.epsl.2010.06.039

Deines, P. (2002) The carbon isotope geochemistry of mantle xenoliths. *Earth-Science Reviews* 58, 247–278. https://doi.org/10.1016/S0012-8252(02)00064-8

Derry, L.A. (2014) 12.9 - Organic Carbon Cycling and the Lithosphere. In: Holland, H.D., Turekian, K.K. (Eds.) *Treatise on Geochemistry*. Second Edition, Elsevier, Amsterdam, 239–249. https://doi.org/10.1016/B978-0-08-095975-7.01014-7

Giuliani, A., Dalton, H., Pearson, D.G. (2025) Kimberlites: The deepest geochemical probes of Earth. In: Anbar, A., Weis, D. (Eds.) *Treatise on Geochemistry*. Third Edition, Volume 1, Elsevier, Amsterdam, 159–230. https://doi.org/10.1016/B978-0-323-99762-1.00064-4

Green, D.H., Wallace, M.E. (1988) Mantle metasomatism by ephemeral carbonatite melts. *Nature* 336, 459–462. https://doi.org/10.1038/336459a0

Hauri, E.H., Maclennan, J., McKenzie, D., Gronvold, K., Oskarsson, N., Shimizu, N. (2018) CO_2 content beneath northern Iceland and the variability of mantle carbon. *Geology* 46, 55–58. https://doi.org/10.1130/G39413.1

Hirschmann, M.M. (2018) Comparative deep Earth volatile cycles: The case for C recycling from exosphere/mantle fractionation of major (H_2O, C, N) volatiles and from H_2O/Ce, CO_2/Ba, and CO_2/Nb exosphere ratios. *Earth and Planetary Science Letters* 502, 262–273. https://doi.org/10.1016/j.epsl.2018.08.023

Horita, J., Polyakov, V.B. (2015) Carbon-bearing iron phases and the carbon isotope composition of the deep Earth. *Proceedings of the National Academy of Sciences* 112, 31–36. https://doi.org/10.1073/pnas.1401782112

Javoy, M., Pineau, F. (1991) The volatiles record of a "popping" rock from the Mid-Atlantic Ridge at 14°N: chemical and isotopic composition of gas trapped in the vesicles. *Earth and Planetary Science Letters* 107, 598–611. https://doi.org/10.1016/0012-821X(91)90104-P

Javoy, M., Pineau, F., Iiyama, I. (1978) Experimental determination of the isotopic fractionation between gaseous CO_2 and carbon dissolved in tholeiitic

magma. A preliminary study. *Contributions to Mineralogy and Petrology* 67, 35–39. https://doi.org/10.1007/BF00371631

Kump, L.R., Arthur, M.A. (1999) Interpreting carbon-isotope excursions: carbonates and organic matter. *Chemical Geology* 161, 181–198. https://doi.org/10.1016/S0009-2541(99)00086-8

Le Voyer, M., Kelley, K.A., Cottrell, E., Hauri, E.H. (2017) Heterogeneity in mantle carbon content from CO_2-undersaturated basalts. *Nature Communications* 8, 14062. https://doi.org/10.1038/ncomms14062

Lee, H., Moussallam, Y., Aubaud, C., Iacono-Marziano, G., Hammond, K., Ebel, D. (2024a) Carbon isotope fractionation between CO_2 and carbon in silicate melts at high temperature. *Geochimica et Cosmochimica Acta* 380, 208–219. https://doi.org/10.1016/j.gca.2024.07.015

Lee, H., Moussallam, Y., Rose Koga, E.F., Piani, L., Villeneuve, J., Bouden, N., Gurenko, A.A., Monteleone, B., Gaetani, G.A. (2024b) High-precision determination of carbon stable isotope in silicate glasses by secondary ion mass spectrometry: Evaluation of international reference materials. *Chemical Geology* 670, 122428. https://doi.org/10.1016/j.chemgeo.2024.122428

Marshall, E.W., Halldórsson, S.A., Tian, L., Jackson, M.G., Jenner, F., Stefánsson, A. (2024) The effect of diffusion on lithium isotope ratios in Icelandic basalts. *Chemical Geology* 662, 122206. https://doi.org/10.1016/j.chemgeo.2024.122206

Mason, E., Edmonds, M., Turchyn, A.V. (2017) Remobilization of crustal carbon may dominate volcanic arc emissions. *Science* 357, 290–294. https://doi.org/10.1126/science.aan5049

Mattey, D.P., Taylor, W.R., Green, D.H., Pillinger, C.T. (1990) Carbon isotopic fractionation between CO_2 vapour, silicate and carbonate melts: an experimental study to 30 kbar. *Contributions to Mineralogy and Petrology* 104, 492–505. https://doi.org/10.1007/BF01575626

Minarik, W.G., Watson, E.B. (1995) Interconnectivity of carbonate melt at low melt fraction. *Earth and Planetary Science Letters* 133, 423–437. https://doi.org/10.1016/0012-821X(95)00085-Q

Moussallam, Y. (2025) Carbon Isotopes in Magmatic Systems: Measurements, Interpretations, and the Carbon Isotopic Signature of the Earth's Mantle. *Geosciences* 15, 266. https://doi.org/10.3390/geosciences15070266

Moussallam, Y., Rose-Koga, E.F., Fischer, T.P., Georgeais, G., Lee, H.J., Birnbaum, J., Pfeffer, M.A., Barnie, T., Regis, E. (2024) Kinetic Isotopic Degassing of CO_2 During the 2021 Fagradalsfjall Eruption and the $\delta^{13}C$ Signature of the Icelandic Mantle. *Geochemistry, Geophysics, Geosystems* 25, e2024GC011997. https://doi.org/10.1029/2024GC011997

Moussallam, Y., Koga, K.T., Rose-Koga, E.F., Aubaud, C., Lee, H.J., Georgeais, G. (2025a) The carbon isotopic signature of the upper mantle is heterogeneous. *Communications Earth & Environment* 6, 6. https://doi.org/10.1038/s43247-024-01973-9

Moussallam, Y., Rose-Koga, E.F., Aubaud, C., Georgeais, G., Cartigny, P., Koga, K.T., Devidal, J.-L., Michael, P.J., Shimizu, K., Saal, A.E. (2025b) Enigmatic carbon isotopic variability in the oceanic upper mantle. *Proceedings of the National Academy of Sciences* 122, e2502886122. https://doi.org/10.1073/pnas.2502886122

Ni, H., Keppler, H. (2013) Carbon in Silicate Melts. *Reviews in Mineralogy and Geochemistry* 75, 251–287. https://doi.org/10.2138/rmg.2013.75.9

Pineau, F., Shilobreeva, S., Hekinian, R., Bideau, D., Javoy, M. (2004) Deep-sea explosive activity on the Mid-Atlantic Ridge near 34°50′N: a stable isotope (C, H, O) study. *Chemical Geology* 211, 159–175. https://doi.org/10.1016/j.chemgeo.2004.06.029

Rohrbach, A., Schmidt, M.W. (2011) Redox freezing and melting in the Earth's deep mantle resulting from carbon–iron redox coupling. *Nature* 472, 209–212. https://doi.org/10.1038/nature09899

Rosenthal, A., Hauri, E.H., Hirschmann, M.M. (2015) Experimental determination of C, F, and H partitioning between mantle minerals and carbonated basalt, CO_2/Ba and CO_2/Nb systematics of partial melting, and the CO_2 contents of basaltic source regions. *Earth and Planetary Science Letters* 412, 77–87. https://doi.org/10.1016/j.epsl.2014.11.044

Saal, A.E., Hauri, E.H., Langmuir, C.H., Perfit, M.R. (2002) Vapour undersaturation in primitive mid-ocean-ridge basalt and the volatile content of Earth's upper mantle. *Nature* 419, 451–455. https://doi.org/10.1038/nature01073

Shea, J., Hughes, E., Balzer, R., Bindeman, I., Blundy, J., Brooker, R., Botcharnikov, R., Cartigny, P., EIMF, Gaetani, G., Kilgour, G., Maclennan, J., Monteleone, B., Neave, D.A., Shortle, O. (2025) Improved Precision and Reference Materials for Stable Carbon Isotope Measurement in Basaltic Glasses using Secondary Ion Mass Spectrometry. *Geostandards and Geoanalytical Research* 49, 607–627. https://doi.org/10.1111/ggr.12610

Stachel, T., Cartigny, P., Chacko, T., Pearson, D.G. (2022) Carbon and Nitrogen in Mantle-Derived Diamonds. *Reviews in Mineralogy and Geochemistry* 88, 809–875. https://doi.org/10.2138/rmg.2022.88.15

Wood, B.J., Li, J., Shahar, A. (2013) Carbon in the Core: Its Influence on the Properties of Core and Mantle. *Reviews in Mineralogy and Geochemistry* 75, 231–250. https://doi.org/10.2138/rmg.2013.75.8

Geochemical Perspectives Letters

A revised carbon isotope composition of the convecting upper mantle

J. Shea, J. Maclennan, M. Edmonds, E. Hughes, M. Hartley, S. Mikhail, M. Perfit, O. Shorttle

Supplementary Information

The Supplementary Information includes:

- Analytical Methods
- Statistical Methods
- Results
- Sample Characterisation
- Kimberlites and Associated Rocks
- Laser Secondary Standards
- Sample Measurements
- Tables S-1 to S-6
- Figures S-1 to S-6
- Supplementary Information References

Analytical Methods

Secondary ion mass spectrometry (SIMS) for CO_2 and $\delta^{13}C$ measurements. Carbon isotope measurements were conducted using a Cameca IMS-1280 large-geometry secondary ion mass spectrometer at the Northeast National Ion Microprobe Facility, Woods Hole Oceanographic Institution, USA, following the analytical protocol of Shea *et al.*, (2025a). Sample preparation involved pressing olivines containing melt inclusions and carbon-free San Carlos Olivines and the ETNA36 and ETNA24 reference materials in indium on one-inch aluminium rounds to avoid carbon contamination from organic epoxy mounting media. All melt inclusions and reference materials were mounted less than 10 mm from the centre of the one-inch mount to avoid deflection artefacts. Analysed melt inclusions are discussed below in Sample Characterisation. A $^{133}Cs^+$ primary beam (10 kV, 10 nA) was rastered over a 25 × 25 µm area for 300 s pre-sputtering, then reduced to 20 × 20 µm measurement, producing a 40 µm analytical pit. Multi-collection simultaneously measured $^{12}C^-$ and $^{13}C^-$ on electron multipliers with $^{18}O^-$ as the reference mass on a Faraday cup detector. Measurements comprised 100 cycles with optimised secondary ion optics achieving mass resolving power of ~5000 to resolve $^1H^{12}C^+$ polyatomic interference on $^{13}C^-$. Calibration employed synthetic basalt reference materials ETNA24 and ETNA36 (CO_2: 2026 – 2300 µg g^{-1}, $\delta^{13}C$: -10.2 and -14.3‰), characterised using step-heating manometry combined with IRMS, combined with lower concentration CO_2 in-house reference materials from Woods Hole Oceanographic Institution. CO_2 concentrations were determined using $^{12}C/^{18}O$ ratios, with oxygen calculated from charge balancing each ion measured by EPMA analysis, with full uncertainty propagation of all ions to ascertain uncertainty on the calculated oxygen. An averaged instrumental mass fractionation (IMF) factor was applied to all measurements.

Background corrections were applied to all measurements to control for mixing with organic carbon contamination as detailed in Shea *et al.* (2025a). Carbon background contamination was minimised to <1 ppm CO_2, with the low background levels resulting in background corrections of typically <1‰ for most samples, enabling reliable $\delta^{13}C$ measurements down to ~6 ppm CO_2. Final CO_2 concentration uncertainties were calculated using orthogonal distance regression to fully propagate all uncertainties from the measurement, calibration, and isotope correction procedures, incorporating the measured isotope ratio, reference mass, and associated uncertainty. Measurement precision under repeatability conditions was typically ±0.35‰ (1 RSE) at high CO2 concentrations, with ±1.00‰ (1 RSE) at moderate levels (163 – 267 μg g^{-1}). All $\delta^{13}C$ values are reported relative to Vienna Pee Dee Belemnite (VPDB) standard. Full analytical details, including calibration curves, are provided in Shea *et al.* (2025a).

Electron probe microanalysis (EPMA). Major element measurements on the melt inclusion glasses were conducted using a JEOL Field Emission Gun (FEG) JXA-iHP200F microprobe in the Department of Earth Sciences at the University of Cambridge. Operating conditions included an accelerating voltage of 15 kV, beam current of 6 nA, and beam diameter of 5 μm, with a take-off angle of 40°. Si, Ti, Al, Cr, Fe, Ni, Mn, Mg, Ca, Na, K, P, and S were measured using wavelength-dispersive spectrometry (WDS) with the following crystal configurations: Si Kα on TAPL, Ti Kα on PETL, Al Kα on TAPL, Cr Kα on LIFL, Fe Kα on LIFL, Ni Kα on LIFL, Mn Kα on LIFL, Mg Kα on TAPL, Ca Kα on PETH, Na Kα on TAP, K Kα on PETL, P Kα on PETL, and S Kα on PETH crystals. Peak counting times were 20 s for Si, Al, Mg, Ca, Na, and K; 40 s for Ti, Cr, and Mn; 60 s for Fe and P; and 150 s for S. Background counting times were 10 s for Si, Al, Mg, Ca, Na, and K; 20 s for Ti, Cr, and Mn; 30 s for Fe and P; and 75 s for S. Calibration was performed using the following certified reference materials and measurement standards: wollastonite (Si), rutile (Ti), K-feldspar (Al, K), Cr metal (Cr), fayalite (Fe), NiO (Ni), Mn metal (Mn), periclase (Mg), diopside (Ca), jadeite (Na), apatite (P), and pyrite (S). Peak and background counting times were optimised for each element to achieve adequate counting statistics whilst minimising measurement drift and beam damage to volatile elements, particularly Na and K. Data reduction was performed using the φ(ρz) matrix correction procedure to account for atomic number, absorption, and fluorescence effects. Measurement precision, assessed from replicate measurements of reference materials under repeatability conditions, was typically <1% relative standard deviation for major elements (Si: 0.31% RSD, Mg: 0.49% RSD) and <3% relative standard deviation for minor elements (Fe: 2.61% RSD). Results are reported as element oxides with measurement totals typically between 99-101 wt%, indicating excellent measurement accuracy and absence of significant matrix effects. Measurement trueness was monitored through regular measurements of an in house Stapafell basalt reference material (STAP; Taracsák *et al.*, 2021). Where possible, multiple measurement points were taken on individual melt inclusions to assess homogeneity, with results reported as weighted averages with propagated measurement uncertainties.

Laser ablation inductively coupled plasma mass spectrometry (LA-ICP-MS). Measurements were conducted on an ESI NWR 193nm excimer laser-ablation system interfaced to a Perkin-Elmer Nexion 350D ICP-MS in the Department of Earth Sciences at the University of Cambridge. Pure helium was used as the ablation gas at a precisely controlled flow rate of 600 mL min^{-1}. The helium flow carrying the ablated sample material was joined with an argon stream from the ICP-MS at 1 L min^{-1} before entering the plasma. Measurements were conducted using a laser repetition rate of 20 Hz and laser fluence of 4 J cm^{-2}. ^{7}Li, ^{11}B, ^{29}Si, ^{43}Ca, ^{44}Ca, ^{45}Sc, ^{47}Ti, ^{51}V, ^{53}Cr, ^{55}Mn, ^{59}Co, ^{60}Ni, ^{65}Cu, ^{66}Zn, ^{69}Ga, ^{74}Ge, ^{85}Rb, ^{88}Sr, ^{89}Y, ^{90}Zr, ^{93}Nb, ^{137}Ba, ^{139}La, ^{140}Ce, ^{141}Pr, ^{143}Nd, ^{147}Sm, ^{153}Eu, ^{157}Gd, ^{159}Tb, ^{163}Dy, ^{165}Ho, ^{166}Er, ^{169}Tm, ^{172}Yb, ^{175}Lu, ^{178}Hf, ^{181}Ta, ^{208}Pb, ^{232}Th, ^{238}U were measured using spot sizes that varied between 60 and 80 μm, depending on the size of the melt inclusions. ^{43}Ca and ^{44}Ca were analysed to monitor potential $^{28}Si^{16}O^{+}$ interference on ^{44}Ca and $^{29}Si^{16}O^{+}$ interference on monoisotopic ^{45}Sc; no interference outside of measurement uncertainty was measured. ^{65}Cu and ^{66}Zn were selected to mitigate any issues with magnesium argide polyatomic interferences. For elements with very high ICP-MS signals (Na, Al, Si), the Nexion RPa and RPq collision/reaction cell parameters were adjusted to attenuate signals and ensure detection on pulse counters, avoiding use of the analogue detector. Measurements lasted 64 s, which included 20 s of background, 30 s of measurement, and 14 s of washout. The measurement standard NIST612 and SiO_2 content measured by EPMA were used for internal standard normalisation, whilst the certified reference material NIST610 was used to measure measurement trueness and uncertainty, and BHVO-2G and BIR-1G were used for quality assurance secondary reference materials (see spreadsheet of laser secondary standards, available for

download from the online version of this article at https://doi.org/10.7185/geochemlet.2610). Measurement precision, based on repeated measurements of NIST610 under repeatability conditions, was on average 6.2% RSD for most elements (ranging from 4.2% for Ho to 12% for Zn; Table S-2). All data were reduced using GLITTER software v4.5 (Griffin *et al.*, 2008). Where elements did not exceed the limit of detection, concentrations are reported as less than the limit of detection, and these measurements were excluded from plots. Where possible, duplicate or triplicate measurements were conducted close to the centre of the melt inclusions, with results reported as weighted mean $\bar{x} = \sum_i(x_i/\sigma_i^2) \,/\, \sum_i(1/\sigma_i^2)$ with propagated measurement uncertainties $SE = \left(\sum_i \sigma_i^{-2}\right)^{-1/2}$, assuming individual measurement uncertainties are independent and no excess scatter beyond measurement uncertainty.

Statistical Methods

All statistical calculations were implemented in Python (version 3.11.6) using NumPy (version 1.26.4) and SciPy (version 1.14.1) libraries (Harris *et al.*, 2020; Virtanen *et al.*, 2020). Weighted means, variance decomposition, and overdispersion statistics were calculated following standard uncertainty propagation and intrinsic variance estimations in physical sciences (Taylor, 1997; Lyons, 1991). Chi-squared values were obtained using `scipy.stats.chi2.ppf()`. Weighted statistics and Monte Carlo simulations were calculated using either custom functions or custom Jupyter notebook implementations with full uncertainty propagation to ensure transparency and reproducibility. Full Python code used for data processing, statistical analysis, and figure generation is provided in Shea *et al.* (2025b).

Weighted mean calculations. For datasets with associated analytical uncertainties, we calculated weighted means using:

$$\bar{x}_w = \frac{\sum_{i=1}^{n} w_i x_i}{\sum_{i=1}^{n} w_i} \tag{S-1}$$

where $w_i = 1/\sigma_i^2$ are the inverse-variance weights derived from the individual analytical uncertainties σ_i. Inverse-variance weighting provides the minimum-variance unbiased estimator of the population mean when measurement uncertainties differ between observations, ensuring that more precise measurements contribute proportionally greater influence on the final estimate (Taylor, 1997; Lyons, 1991). This approach is standard practice where heteroscedastic uncertainties are present.

Z-score calculation and overdispersion assessment. For each dataset, we calculated normalised residuals (z-scores) as:

$$z_i = \frac{x_i - \bar{x}_w}{\sigma_i}, \tag{S-2}$$

where x_i are individual $\delta^{13}C$ measurements, $\bar{x}_w$ is the weighted mean, and σ_i are the individual measurement uncertainties.

The standard deviation of the z-scores was used to assess overdispersion:

$$\sigma_z = \sqrt{\frac{1}{n-1}\sum_{i=1}^{n}\left(\frac{x_i - \bar{x}_w}{\sigma_i}\right)^2} = \sqrt{\frac{1}{n-1}\sum_{i=1}^{n} z_i^2}. \tag{S-3}$$

The factor $(n-1)$ accounts for the loss of one degree of freedom associated with estimating the population mean from the data. This correction, known as Bessel's correction, ensures an unbiased estimate of the population variance when the mean is estimated from the sample rather than known *a priori* (Taylor, 1997; Lyons, 1991).

If analytical uncertainty fully accounts for the observed scatter, these normalised residuals should follow a standard normal distribution with unit variance (Taylor, 1997). Under this condition, σ_z is expected to approximate 1.0. Values of $\sigma_z > 1.0$ indicate excess variance beyond analytical uncertainty, reflecting intrinsic natural heterogeneity in

the mantle source, whereas values of $\sigma_z < 1.0$ indicates that analytical uncertainty fully explains the observed scatter (Taylor, 1997; Lyons, 1991).

Statistical significance of overdispersion. To determine whether observed overdispersion reflects genuine natural heterogeneity rather than sampling variability, we performed a chi-squared test of the normalised residual variance. Under the null hypothesis that $\sigma_z = 1.0$ (i.e., all observed scatter is fully explained by analytical uncertainty), the test statistic:

$$\chi^2 = (n-1) \cdot \sigma_z^2, \tag{S-4}$$

follows a chi-squared distribution with $\nu = (n - 1)$ degrees of freedom (Taylor, 1997; Lyons, 1991). The use of $\nu = n - 1$ degrees of freedom reflect the estimation of the population mean from the data, which introduces one fitted parameter and reduces the number of independent degrees of freedom accordingly (Taylor, 1997; Lyons, 1991). The corresponding p-value is calculated as the probability of observing a chi-squared value greater than or equal to the observed value under the null hypothesis. Critical values were evaluated at the $\alpha = 0.05$ significance level and were calculated using `scipy.stats.chi2.ppf()`. Only datasets where the calculated χ^2 exceeded the critical value (equivalently, where $p < 0.05$) were considered to show statistically significant overdispersion, indicating intrinsic natural heterogeneity beyond analytical uncertainty rather than purely analytical scatter (Taylor, 1997; Lyons, 1991).

Variance decomposition and natural heterogeneity quantification. For datasets showing statistically significant overdispersion, we performed variance decomposition analysis to separate analytical uncertainty from geological signal. The total observed variance can be partitioned into analytical and natural components:

$$\sigma^2_{\text{total}} = \sigma^2_{\text{analytical}} + \sigma^2_{\text{natural}}, \tag{S-5}$$

where $\sigma_{\text{analytical}}$ represents measurement uncertainty and σ_{natural} represents intrinsic mantle heterogeneity (Taylor, 1997).

The overdispersion statistic (σ_z; Eq. S-3) quantifies how much the observed scatter exceeds analytical uncertainty alone. A value of $\sigma_z > 1$ indicates additional natural variability. The natural variance component can therefore be calculated directly from the excess variance:

$$\sigma^2_{\text{excess}} = (\sigma_z^2 - 1)\sigma^2_{\text{analytical}}. \tag{S-6}$$

This relationship shows that the excess scatter beyond analytical uncertainty reflects true mantle heterogeneity (Lyons, 1991). The relative magnitude of natural variability compared to analytical uncertainty is given by the ratio of their standard deviations:

$$\frac{\sigma_{\text{natural}}}{\sigma_{\text{analytical}}} = \sqrt{\sigma_z^2 - 1}. \tag{S-7}$$

To express this in absolute units (‰), we multiplied this ratio by the average analytical uncertainty for the undegassed dataset:

$$\sigma_{\text{natural}} = \sqrt{\sigma_z^2 - 1}\bar{\sigma}_{\text{analytical}}. \tag{S-8}$$

The fraction of total variance attributable to natural heterogeneity and analytical uncertainty are therefore:

$$f_{\text{natural}} = \frac{\sigma^2_{\text{natural}}}{\sigma^2_{\text{total}}} = \frac{\sigma_z^2 - 1}{\sigma_z^2} = 1 - \frac{1}{\sigma_z^2}, \tag{S-9}$$

and

$$f_{\text{analytical}} = \frac{\sigma^2_{\text{analytical}}}{\sigma^2_{total}} = \frac{1}{\sigma_z^2}, \tag{S-10}$$

such that

$$f_{natural} + f_{analytical} = 1.$$

Therefore, this approach provides a quantitative estimate of the natural mantle heterogeneity independent of measurement precision (Taylor, 1997; Lyons, 1991).

Monte Carlo simulation of fractional organic carbon burial (f_{org}). The fraction of organic carbon burial (f_{org}) was estimated using a Monte Carlo simulation implemented in Python using NumPy and SciPy (Harris *et al.*, 2020; Virtanen *et al.*, 2020), following standard uncertainty propagation approaches (Taylor, 1997; Press *et al.*, 2007). The calculation is based on the steady-state carbon isotope mass balance between organic and carbonate carbon reservoirs:

$$\delta^{13}C_{in} = \delta^{13}C_{org}f_{org} + \delta^{13}C_{carb}(1 - f_{org}), \quad \text{(S-11)}$$

rearranged to solve for f_{org}:

$$f_{org} = \frac{\delta^{13}C_{in} - \delta^{13}C_{carb}}{\delta^{13}C_{org} - \delta^{13}C_{carb}}. \quad \text{(S-12)}$$

Monte Carlo sampling was used to propagate uncertainty in all parameters. We performed 10^6 random Monte Carlo draws, sampling $\delta^{13}C_{in}$ from a normal distribution with mean -3.6‰ and standard deviation SD 0.1‰, derived from the 95% confidence interval of the convecting upper mantle estimate ($\sigma = CI/1.96$). For comparison with previous mantle estimates, we also performed simulations using -4.9 ‰ ± 1.9‰ (SD) from Stachel *et al.* (2022).

Carbonate carbon isotope compositions ($\delta^{13}C_{carb}$) were sampled from a normal distribution with mean 0‰ and standard deviation 0.5‰ to account for natural carbonate heterogeneity. Organic carbon isotope compositions ($\delta^{13}C_{org}$) were generated by applying a biologically derived fractionation factor sampled from a truncated normal distribution (mean -26‰, SD 2‰, truncated between -30‰ and -20‰), consistent with observed biological fractionation ranges (Kump and Arthur, 1999).

Only physically realistic solutions were retained, requiring $0 \leq f_{org} \leq 1$ and denominators ($\delta^{13}C_{org}$ - $\delta^{13}C_{carb}$) sufficiently distinct from zero to avoid numerical instabilities. The resulting f_{org} distributions were used to calculate median values and confidence intervals, and results are shown in Figures S-5 and S-6.

Results

Collated measurements and their uncertainties can be found in the Borgarhraun, Siqueiros and Glasses .csv files (available for download from the online version of this article at https://doi.org/10.7185/geochemlet.2610).

Degassed population. Degassed samples were identified by statistical outliers of $\delta^{13}C$ values from melt inclusion and embayment measurements. We assumed that most melt inclusions and embayments represent undegassed magmatic compositions, with outliers representing degassed samples.

For each volcano, a weighted mean $\delta^{13}C$ was calculated using melt inclusions and embayments (matrix glass excluded). Samples with a z-score > 3.0 were identified as a possible degassed population, based on the assumption most samples were not degassed and a z-score > 3.0 indicates >99% deviation from the population mean. This approach is validated by outliers showing more negative $\delta^{13}C$ values that align with open-system equilibrium degassing model trends. Degassed samples are plotted as red diamonds in the main text on Figure 2.

Upper mantle $\delta^{13}C$. After removing degassed measurements, we calculated refined $\delta^{13}C$ statistics for the undegassed population to estimate the primary mantle carbon isotope signature. This approach isolates samples that best represent the initial magmatic composition prior to significant CO_2 degassing and associated isotope fractionation.

Overdispersion and its statistical significance. The variance decomposition analysis reveals that the excess variance ratio ($\sigma_z^2 - 1$) = 0.56, corresponding to a natural-to-analytical variance ratio of 0.56. This implies that 36% of the total variance is attributable to natural heterogeneity beyond analytical uncertainty. With an average analytical uncertainty of 1.05‰ (1σ), this corresponds to a natural mantle heterogeneity component of 0.79‰ (1σ), compared to a total observed standard deviation of 1.31‰.

For the combined undegassed dataset (n=78) the σ_z = 1.25, χ^2 = 120.43, α = 98.48, and a p-value = 0.0011. Since $\chi^2 > \alpha$ and p = 0.0011 < 0.05, we reject H_0 at the 95% confidence interval, demonstrating that natural heterogeneity in the mantle source contributes to the variance observed in our dataset.

Sample Characterisation

Principal component analysis (PCA) of melt inclusion chemistry. To check from bias in how our location sample locations record upper mantle $\delta^{13}C$ and how the olivines entrapped the enclosed melt inclusions, PCA was performed separately on the geochemical datasets from Borgarhraun and Siqueiros to identify patterns of element covariation and reduce data dimensionality. Prior to analysis, samples with missing data were excluded, and the following variables were removed from the analysis: sample identifiers (sample, olivine_id), categorical variables (sample_type, Location), elements with high analytical uncertainty or below detection limits (Cr_2O_3, NiO, P_2O_5, TiO_2), analytical totals (Total), and calculated oxygen values (O).

Data preprocessing followed standard procedures for compositional geochemical data. All remaining major and trace element concentrations were standardised to zero mean and unit variance using z-score normalisation to ensure equal weighting of variables regardless of their absolute concentration ranges or measurement units. This standardisation step is essential for PCA to prevent elements with higher absolute values from dominating the principal components. PCA was implemented using the scikit-learn decomposition module in Python (Pedregosa *et al.*, 2011), with two principal components extracted for each dataset. The choice of two components was based on interpretability and the requirement to capture the primary patterns of element covariation while maintaining sufficient variance explanation. Standardised data were transformed using `StandardScaler()` prior to fitting the PCA model.

For each dataset, we calculated: (1) principal component loadings for PC1 and PC2, representing the contribution of each element to the respective components; (2) explained variance ratios for each component; (3) sample scores representing the projection of each sample onto the principal component space; and (4) loading angles in PC1-PC2 space, calculated as $\theta = arctan(PC2\ loading/PC1\ loading)$ and converted to degrees, to quantify the angular relationships between elements in the reduced dimensional space.

The geological interpretation of principal components was based on the pattern of element loadings, with particular attention to known element associations and partitioning behaviours in basalt systems and olivine-hosted melt inclusions. Elements with similar loading patterns (small angular differences) were interpreted as geochemically coherent, while orthogonal relationships indicated independent geochemical behaviour.

Melt inclusion chemistry characterisation. To investigate whether different magmatic processes could introduce systematic bias in $\delta^{13}C$ measurements, we examined PCA-ordered element covariance patterns in olivine-hosted melt inclusions and embayments from both locations (Figure S-1). The PCA covariance structures reveal contrasting magmatic controls: Borgarhraun shows strong covariance among lithophile elements and incompatible trace elements, indicating the concurrent mixing of diverse fractional melts during olivine crystallisation; Siqueiros displays weaker inter-element correlations, consistent with efficient pre-entrapment melt homogenisation in the axial magma lens (Maclennan *et al.*, 2003a, 2003b; Rubin *et al.*, 2009; Rudge *et al.*, 2013). Despite these fundamentally different petrogenetic processes, $\delta^{13}C$ shows little correlation with any individual elements at both sites, indicating no systematic bias from variable degree and depth of melting, magmatic evolution, or inclusion entrapment mechanisms. Importantly, CO_2 has strong correlations with other incompatible, non-volatile, trace element concentrations (Ba, Nb, K_2O, La; Figure S-2; Saal *et al.*, 2002; Le Voyer *et al.*, 2017; Hirschmann, 2018; Miller *et al.*, 2019), confirming that both suites record variably undersaturated melts unaffected by degassing that reflect mantle melting. These relationships are further supported by primitive mantle-normalised REE patterns (Figure S-3) and demonstrate that while the Siqueiros and Borgarhraun sample sets do show distinct magmatic evolution pathways, these have not systematically affected the carbon isotope compositions of their trapped liquids.

Some melt inclusions from both Borgarhraun and Siqueiros contained bubbles, which could potentially indicate post-entrapment CO_2 loss. However, we observe no evidence for degassing or CO_2 loss in our dataset. CO_2/ITE ratios are controlled by source composition, and degassing would decouple volatile (CO_2) from non-volatile (Ba, Nb) incompatible trace elements, producing elevated ITE concentrations at anomalously low CO_2 contents. This degassing signature is clearly visible in the uncorrected data from Hauri *et al.* (2018), where samples plot at high Ba concentrations with depleted CO_2 (Figure S-3). In contrast, our Borgarhraun data align with the corrected Hauri *et al.* (2018) values, and our Siqueiros data are consistent with Saal *et al.* (2002), both showing positive correlations between CO_2 and

incompatible trace elements (Figure S-3). The absence of samples plotting at high ITE and low CO_2 demonstrates that our melt inclusions have retained their primary CO_2 concentrations, and any bubbles present likely formed during cooling and decompression after trapping rather than through syn-entrapment or post-entrapment CO_2 loss.

Kimberlites and Associated Rocks

Kimberlites and related melts have a wide $\delta^{13}C$ range observed in (-1.2 to -10.8‰) can largely be explained by degassing of a mantle-derived carbon reservoir. The example open- and closed-system models reproduce the main spread in the data, indicating that progressive CO_2 loss with isotope fractionation is sufficient to account for most observations. Although the specific trajectory depends on starting CO_2 and degassing conditions, the overall array is consistent with convecting upper mantle carbon as the dominant source, and partial degassing driving negative values. A minority of samples with unusually high $\delta^{13}C$ values plot above the mantle field and cannot be generated by degassing, implying an additional contribution from isotopically heavy carbonates.

Supplementary Tables

Table S-1 Evaluation of measurement trueness for EPMA analysis against reference quality values for the STAP glass (Taracsák *et al.*, 2021). Measurement performance metrics are calculated from 38 replicate spot analyses under repeatability conditions of measurement (24 for Cr_2O_3, 7 for NiO). Bias (%) represents the relative difference between measured and reference values, calculated as $(\boldsymbol{measured - reference})/\boldsymbol{reference} \times \mathbf{100}$. The En number (normalised error) is calculated as $\boldsymbol{E_n = |measured - reference|/\sqrt{SEM^2 + \sigma_{ref}^2}}$, where U represents the 2σ uncertainty for each value; $E_n < 1$ indicating agreement within combined uncertainties. Nine of 11 elements achieve En < 1. Biases range from -1.5% (MnO) to +2.2% (TiO_2), all within acceptable limits for routine analysis (±5%). The analytical total (sum of measured oxides) is 100.9% of the reference total, confirming excellent overall calibration, demonstrating that systematic biases are minimal, and overall measurement trueness. Al_2O_3 shows $E_n = 4.5$, reflecting a small systematic positive bias (+2.1%), relative to a very tight combined measurement uncertainty (2σ = 0.06 wt%). MgO (E_n = 1.1) and TiO_2 (E_n = 1.0) marginally exceed or meet the $E_n < 1$ criterion but demonstrate acceptable measurement trueness with biases ≤ 2.3%. Cr_2O_3 and NiO lack reference quantity values as they were not reported in the original characterisation; detection frequencies were 63% (n=24/38) and 18% (n=7/38), respectively, with statistics calculated only from measurements exceeding detection limits.

Oxide	Mean	RSD	2σ	n	Taracsák *et al.* (2021)	2σ	Bias (%)	E_n number
SiO_2	49.25	0.54	0.53	38	48.90	1.30	0.73	0.27
TiO_2	1.657	1.3	0.043	38	1.62	0.04	2.2	1.0
Al_2O_3	14.93	0.64	0.19	38	14.63	0.06	2.1	4.5
Cr_2O_3	0.056	23	0.026	24	-	-	-	-
FeO	10.89	2.5	0.54	38	10.79	0.10	0.92	0.75
NiO	0.0390	6.7	0.0052	7	-	-	-	-
MnO	0.187	10	0.038	38	0.19	0.02	-1.5	0.15
MgO	8.344	0.86	0.14	38	8.22	0.11	1.5	1.1
CaO	12.041	0.59	0.14	38	12.11	0.09	-0.57	0.74
Na_2O	2.10	6.6	0.28	38	2.06	0.12	2.0	0.31
K_2O	0.285	8.0	0.046	38	0.28	0.01	1.8	0.40
P_2O_5	0.214	7.6	0.033	38	0.21	0.04	1.7	0.086
SO_3	0.134	13	0.035	38	0.13	0.02	1.1	0.079

Table S-2 Evaluation of measurement trueness for LA-ICP-MS analysis of NITS SRM 612 glass against reference quantity values from GeoRem (Jochum *et al.*, 2011). Performance metrics calculated from 27 replicate measurements under repeatability conditions of measurement. Bias and E_n number are calculated as described in Table S-1. Overall measurement trueness is excellent, with the average measured analytical sum 101.9% compared to the sum of GeoRem elements, indicating a slight positive bias. Individual element bias ranges from -9.8% (Ge) to +9.1% (Ti), with all values within an acceptable ±10% range for trace element analysis. Twenty-three of 38 elements (61%) achieve $E_n < 1$, demonstrating good agreement within combined uncertainties. Elements with $E_n > 1$ predominantly show small positive biases (3-6%), typical for LA-ICP-MS and potentially reflecting minor matrix effects or instrumental fractionation. The E_n criterion is particularly stringent for elements with very tight GeoRem uncertainties (e.g., Rb, Sr, Pb, Th, U: ±1 μg g^{-1}), where small absolute biases become statistically significant. Rare earth elements demonstrate consistent measurement trueness across the entire suite with biases of -2% to +6%, confirming robust trace element analysis.

Oxide	Mean	RSD	95% CI	n	GeoRem	95% CI	Bias (%)	E_n number
Li	452.8	4.6	8.3	27	468	24	-3.2	0.60
B	327.3	4.7	6.0	27	350	56	-6.5	0.40
Sc	440	11	19	27	455	10	-3.3	0.70
Ti	493	9	18	27	452	10	9.1	1.99
V	444	7	13	27	450	10	-1.3	0.37
Cr	425	6	11	27	408	10	4.2	1.14
Mn	443	9	15	27	444	13	-0.2	0.05
Co	424	7	12	27	410	10	3.4	0.90
Ni	451	8	14	27	458.7	4.0	-1.7	0.53
Cu	447	6.5	11	27	441	15	1.4	0.32
Zn	489	12	23	27	460	18	6.3	0.99
Ga	419	8	13	27	433	13	-3.2	0.76
Ge	403.2	5	7.3	27	447	78	-9.8	0.56
Rb	439	9.0	16	27	425.7	1.0	3.1	0.83
Sr	514	8.6	18	27	515.5	1.0	-0.3	0.08
Y	478	7	14	27	462	11	3.5	0.90
Zr	467.7	5	8.8	27	448	9	4.4	1.57
Nb	478.3	5	9.9	27	465	34	2.9	0.38
Ba	467	6.1	11	27	452	9	3.3	1.06
La	456	5.7	10	27	440	10	3.6	1.13
Ce	456	5.7	10	27	453	8	0.7	0.23
Pr	448.2	4.7	8.3	27	448	7	0.0	0.02
Nd	452.7	4.4	7.8	27	430	8	5.3	2.03
Sm	467.7	5.0	9.3	27	453	11	3.2	1.02
Eu	461.4	3.9	7.1	27	447	12	3.2	1.03

Table S-2 continued.

Oxide	Mean	RSD	95% CI	n	GeoRem	95% CI	Bias (%)	E_n number
Gd	460.6	4.7	8.6	27	449	12	2.6	0.79
Tb	462.6	5	8.3	27	437	9	5.9	2.09
Dy	463.4	4.5	8.2	27	437	11	6.0	1.92
Ho	473.0	4.2	7.8	27	449	12	5.3	1.68
Er	471	5.4	10	27	455	14	3.5	0.93
Tm	448.9	5.4	9.7	27	435	10	3.2	1.00
Yb	441.6	4	7.8	27	450	9	-1.9	0.71
Lu	460.4	5	9.6	27	439	8	4.9	1.71
Hf	453.8	4	7.5	27	435	12	4.3	1.33
Ta	459	5.8	11	27	446	33	2.9	0.37
Pb	443	7.1	12	27	426	1	4.0	1.41
Th	474	5.5	10	27	457.2	1	3.7	1.67
U	460.4	5.3	9.7	27	461.5	1	-0.2	0.11

Table S-3 $\delta^{13}C$ Statistical analysis of samples from each Location and combined statistics.

Location	Weighted Mean $\delta^{13}C$ (‰)	Weighted Mean 1σ (‰)	n	Z-score σ (‰)	Z-score 95% CI (‰)
Borgarhraun	-3.6	1.5	49	1.6	1.3-2.0
Siqueiros	-3.7	1.6	30	1.3	1.0-1.7
Combined	-3.7	1.6	73	1.5	1.3-1.8

Table S-4 $\delta^{13}C$ Statistics for undegassed samples only. Combined population 95% Confidence Interval: -3.76 to -3.35‰.

Location	Weighted Mean $\delta^{13}C$ (‰)	Standard Error (‰)	95% CI (‰)	n	Weight (%)
Borgarhraun	-3.52	0.12	± 0.24‰	47	75.8
Siqueiros	-3.66	0.22	± 0.43‰	31	24.2
Combined	-3.55	0.11	± 0.21‰	78	100

Table S-5 Principal component analysis loadings for Borgarhraun melt inclusion geochemistry. Element loadings for the first two principal components, with loading angles quantifying angular relationships in PC1-PC2 space. Elements with similar loading angles exhibit geochemically coherent behaviour. Data were standardised (zero mean, unit variance) prior to analysis. PC1 explains 46.8% of variance (eigenvalue = 23.70); PC2 explains 18.5% of variance (eigenvalue = 9.40); cumulative variance explained = 65.3%. n = 49 elements. Elements are ordered by loading angle.

Element	PC1 Loading	PC2 Loading	Loading Angle (°)
Al_2O_3	-0.116	-0.084	-143.9
MnO	0.03	-0.189	-81.1
Cu	0.013	-0.081	-80.6
FeO	0.044	-0.221	-78.7
Na_2O	0.074	-0.227	-71.8
Pb	0.026	-0.063	-67.4
Li	0.125	-0.225	-60.8
Zn	0.141	-0.172	-50.6
Tb	0.169	-0.174	-45.7
Co	0.109	-0.108	-44.9
Dy	0.167	-0.163	-44.4
Ho	0.17	-0.167	-44.4
Mn	0.153	-0.131	-40.5
Y	0.178	-0.147	-39.5
Er	0.175	-0.144	-39.3
Tm	0.168	-0.131	-38
Yb	0.171	-0.122	-35.6
Ge	0.025	-0.016	-33.7
Ti	0.188	-0.112	-30.9
Eu	0.186	-0.11	-30.7
Gd	0.177	-0.101	-29.8
B	0.076	-0.039	-26.9
Lu	0.171	-0.076	-23.9
Sm	0.184	-0.08	-23.6
Ga	0.167	-0.056	-18.4
V	0.187	-0.017	-5.3
Sc	0.177	0.005	1.6
Ni	0.093	0.008	5.2
Zr	0.194	0.035	10.1
Nd	0.197	0.045	13
$\delta^{13}C$	0.045	0.012	15.2
Hf	0.186	0.071	20.8
Sr	0.165	0.083	26.8
Pr	0.188	0.106	29.3
Cr	0.13	0.081	31.8
Ce	0.18	0.146	39.1
La	0.17	0.18	46.6

Table S-5 continued.

Element	PC1 Loading	PC2 Loading	Loading Angle (°)
SO_3	0.116	0.133	48.9
Nb	0.161	0.186	49.1
Th	0.143	0.212	56.1
K_2O	0.134	0.202	56.4
Ba	0.147	0.225	56.8
Ta	0.145	0.225	57.2
U	0.135	0.212	57.6
Rb	0.132	0.232	60.4
CO_2	0.098	0.218	65.8
CaO	0.064	0.205	72.6
MgO	-0.025	0.105	103.3
SiO_2	-0.048	0.006	172.6

Table S-6 Principal component analysis loadings for Siqueiros melt inclusion geochemistry. Element loadings for the first two principal components, with loading angles quantifying angular relationships in PC1-PC2 space. Elements with similar loading angles exhibit geochemically coherent behaviour. Data were standardized (zero mean, unit variance) prior to analysis. PC1 explains 27.0% of variance (eigenvalue = 13.67); PC2 explains 18.5% of variance (eigenvalue = 9.37); cumulative variance explained = 45.5%. n = 48 elements. Elements are ordered by loading angle.

Element	PC1 Loading	PC2 Loading	Loading Angle (°)
MgO	-0.143	-0.018	-172.9
Cu	-0.153	-0.029	-169.2
MnO	-0.084	-0.114	-126.4
Na_2O	0.203	-0.13	-32.7
Tm	0.193	-0.101	-27.7
Ti	0.207	-0.109	-27.7
Nd	0.184	-0.067	-20
Cr	0.163	-0.05	-17
SiO_2	0.153	-0.045	-16.6
Tb	0.236	-0.061	-14.5
Eu	0.235	-0.043	-10.4
Sm	0.209	-0.021	-5.8
Sc	0.203	-0.009	-2.5
$\delta^{13}C$	0.029	-0.001	-1.7
Ge	0.078	-0.001	-0.9
Yb	0.231	0.004	0.9
Y	0.248	0.009	2
Dy	0.249	0.012	2.7
Er	0.216	0.012	3.2
SO3	0.151	0.009	3.3
Ho	0.241	0.031	7.3
Lu	0.181	0.032	10.1
Hf	0.109	0.032	16.1
Pb	0.032	0.017	27.7

Table S-6 continued.

Element	PC1 Loading	PC2 Loading	Loading Angle (°)
V	0.154	0.107	34.9
Zr	0.151	0.118	38
Ga	0.205	0.176	40.7
CaO	0.076	0.066	41.2
Al_2O_3	0.069	0.073	46.8
Zn	0.126	0.175	54.2
Mn	0.095	0.142	56.2
Pr	0.103	0.181	60.5
Li	0.057	0.102	60.9
Th	0.064	0.25	75.6
B	0.044	0.182	76.3
U	0.025	0.301	85.3
Ta	0.001	0.248	89.9
Nb	-0.01	0.308	91.8
CO_2	-0.006	0.163	92.2
Rb	-0.012	0.242	92.9
Ba	-0.025	0.236	96
Ce	-0.03	0.275	96.2
La	-0.059	0.299	101.2
Sr	-0.071	0.241	106.5
K_2O	-0.088	0.226	111.3
FeO	-0.081	0.074	137.5
Co	-0.087	0.068	142.1
Ni	-0.12	0.009	175.8

Supplementary Figures

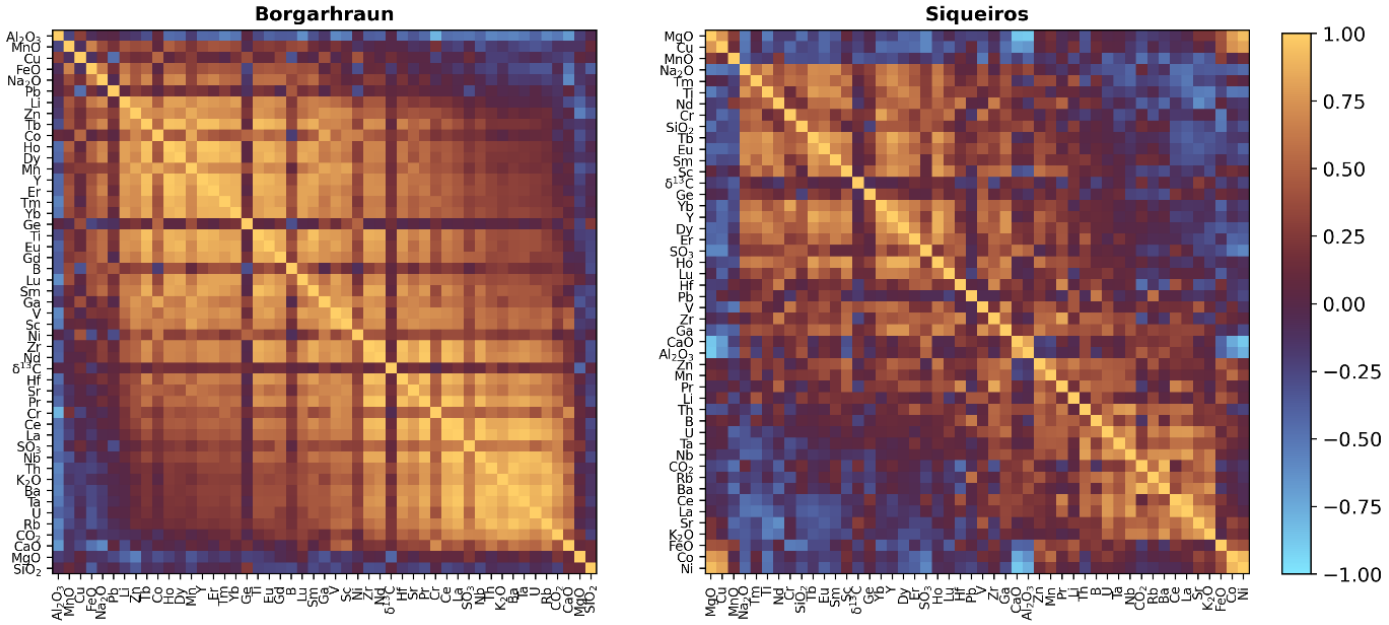

Figure S-1 Correlation matrices for olivine-hosted melt inclusions from Borgarhraun (Iceland; left) and Siqueiros (EPR; right), with elements ordered by PCA loading angle in PC1–PC2 space. Elements are ordered by PCA loading angle so that geochemically similar elements are adjacent; this ordering reveals contiguous square regions of strong positive correlation (*'block structure'*) along the diagonal, which represent element groups that vary coherently due to shared petrogenetic controls. Strong block structure indicates systematic compositional evolution, whereas weak or diffuse structure reflects efficient pre-entrapment homogenisation. Borgarhraun shows strong block structures and high variance explained (PC1 = 46.0%, PC2 = 19.4%), consistent with systematic fractional melt mixing and crystallisation during olivine growth. Siqueiros, by contrast, has weaker block structure and lower variance explained (PC1 = 25.7%, PC2 = 18.8%), reflecting efficient pre-entrapment mixing that homogenised REE patterns, leaving residual variance from minor source heterogeneity and post-entrapment modification (Ni, Co, FeO, MgO, Cu MnO diffusion into the surrounding olivine). The absence of correlation between $\delta^{13}C$ and any other element confirms that carbon isotope composition varies independently of melt evolution, fractional crystallisation, and incompatible element enrichment in both locations.

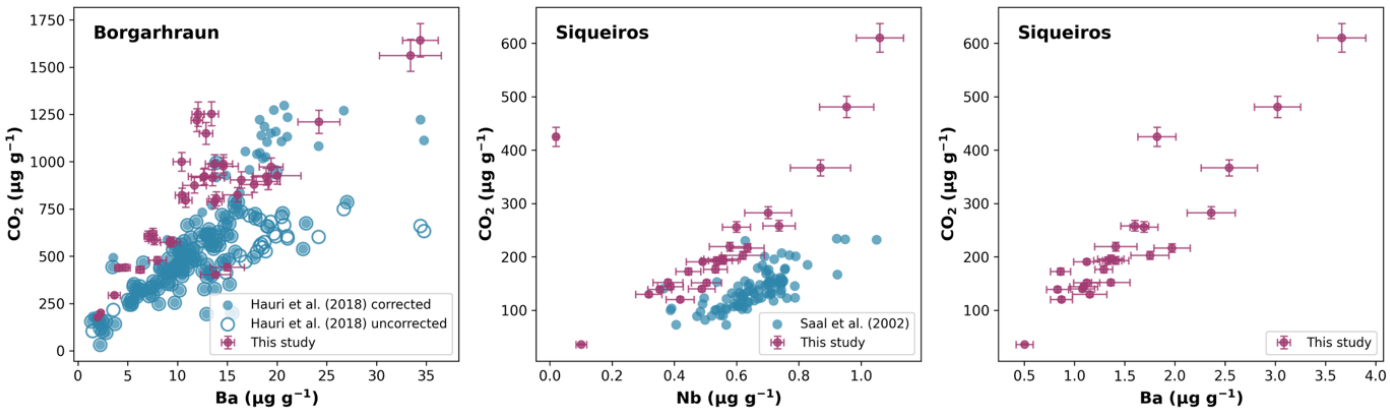

Figure S-2 Coupled CO_2 and incompatible trace element (Ba and Nb) variations in Borgarhraun and Siqueiros melt inclusions do not indicate degassing. (a) CO_2 versus Ba concentrations for Borgarhraun melt inclusions (purple circles, this study) compared with data from Hauri *et al.* (2018) shown as corrected (corrected for CO_2 degassing; filled blue circles) and uncorrected (raw measurements; open blue circles) values. (b) CO_2 versus Nb concentrations for Siqueiros melt inclusions (purple circles, this study) compared with data from Saal *et al.* (2002) (filled blue circles). (c) CO_2 versus Ba concentrations for Siqueiros melt inclusions (purple circles, this study). CO_2/ITE ratios are controlled by source composition. Degassing would decouple CO_2 from non-volatile trace elements, producing high ITE concentrations with low CO_2, as seen in the uncorrected Hauri *et al.* (2018) data. Our data align with corrected literature values and show no evidence of degassing, while Nb and Ba show coupled increases with CO_2, confirming that the measured CO_2 concentrations are preserved primary carbon values and consistent with previous findings. Uncertainty bars represent 1σ analytical uncertainties.

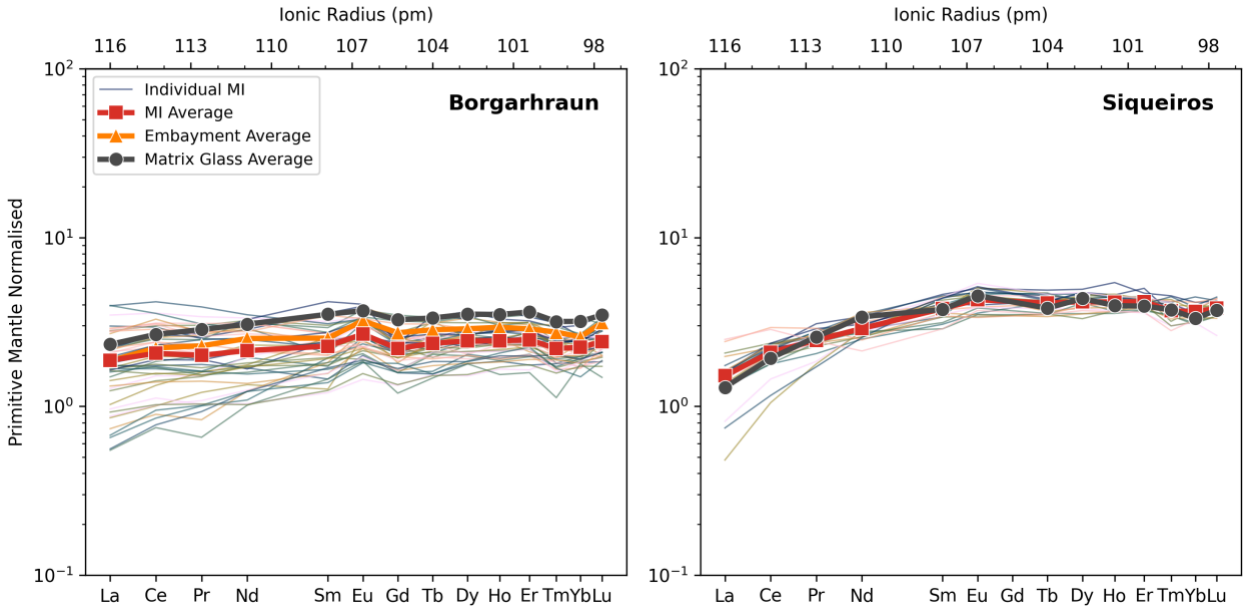

Figure S-3 Primitive mantle–normalised rare earth element (REE) variation diagrams for olivine-hosted basaltic melt inclusions and their host matrix glasses from Borgarhraun (left) and Siqueiros (right). Individual melt inclusion measurements are shown as thin coloured lines, with averaged melt inclusion compositions displayed as red lines with square symbols**.** Embayment averages are shown as orange lines with triangular symbols (Borgarhraun only). Matrix glass compositions are shown as grey lines with circular symbols. REE concentrations are normalised to primitive mantle values from Palme and O'Neill (2014) and plotted against ionic radius (secondary x-axis). At Borgarhraun, light REEs (La–Nd) show moderate variability amongst melt inclusions, whereas heavy REEs (Gd–Lu) display less variability. The systematic increase in REE concentrations from melt inclusion average through embayment average to matrix glass demonstrates progressive fractional crystallisation from magma storage to ascent and eruption. In contrast, Siqueiros inclusions exhibit overall lower variability than those from Borgarhraun, with relative depletion in light REEs (La–Nd) compared to middle and heavy REEs, consistent with derivation from a depleted mantle source. The averaged composition closely matches the matrix glass, indicating minimal fractional crystallisation or efficient melt homogenisation. The host glass compositions illustrate the integrated mixtures of the input fractional melts in the erupted lavas at both locations. The embayment compositions at Borgarhraun provide direct evidence for intermediate stages of magmatic evolution, contrasting with the more primitive signatures preserved at Siqueiros. These observations are consistent with the PCA-informed correlation matrices in Figure S-1, which highlight efficient pre-crystallisation melt mixing at Siqueiros versus mixing concurrent with olivine crystallisation at Borgarhraun.

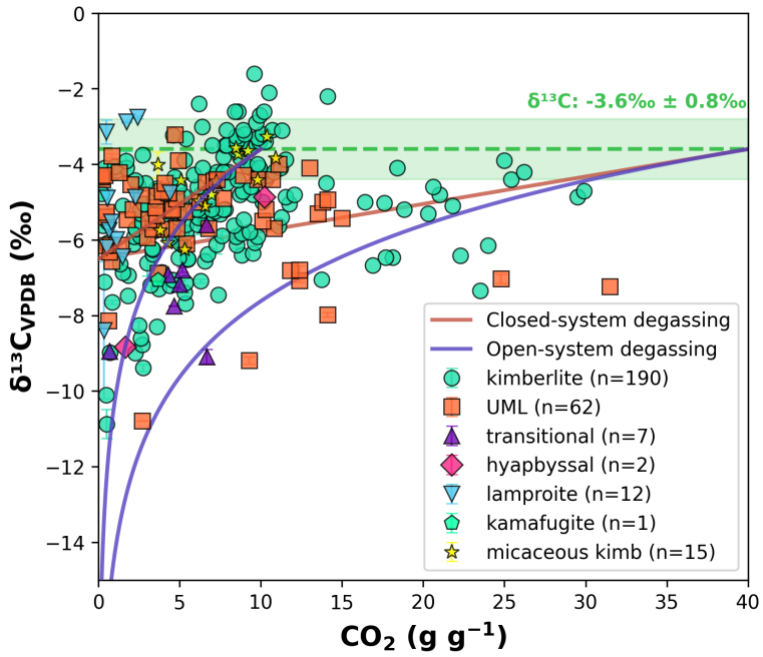

Figure S-4 $\delta^{13}C$ versus CO_2 for kimberlites and related ultramafic melts (global compilation from Giuliani *et al.*, 2025). The green shaded band shows the revised convecting mantle value ($\delta^{13}C$ = -3.55 ± mantle heterogeneity of 0.79‰). Example open- (purple) and closed-system (red) degassing trajectories are shown for different initial CO_2 contents (sample as Figure 2), with arbitrary 10% and 40% starting concentrations for illustrative purposes. Most data fall along or between these trajectories, consistent with mantle-derived carbon undergoing partial degassing during ascent. Rare heavy outliers (>-2.26‰) lie above the mantle field and cannot be reproduced by degassing alone, requiring an additional isotopically heavy component such as recycled carbonate. Model curves are illustrative and demonstrate plausibility rather than unique histories, as trajectories vary with starting CO_2 content, fractionation factors (+2.9‰ from basaltic systems is used here; Lee *et al.*, 2024), and ascent conditions.

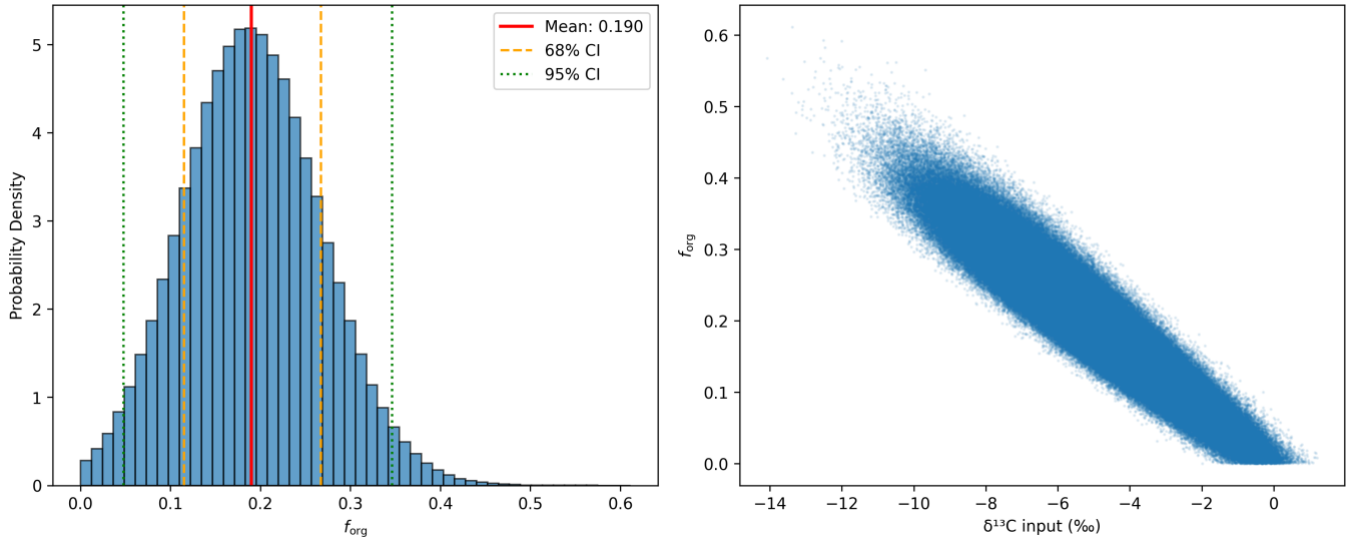

Figure S-5 Monte Carlo analysis of fractional organic carbon burial (f_{org}) using revised mantle carbon isotope composition. (Left) Probability density histogram showing the distribution of f_{org} values with mean = 0.137 (13.7%, red line), 68% confidence intervals (11.6-16.0%, orange dashed lines), and 95% confidence intervals (10.0-19.2%, green dotted lines). (Right) Scatter plot illustrating the inverse relationship between $\delta^{13}C$ input values and calculated f_{org}, with point density reflecting the underlying parameter distributions. The elliptical pattern demonstrates how uncertainties in mantle carbon isotope composition propagate through the mass balance calculation. The results demonstrate that revised mantle endmember values yield $f_{org} = 13.7^{+2.3}_{-2.1}\%$, consistent with sedimentary inventory approaches (10-17%) rather than past isotopic estimates (19-34%; Derry, 2014).

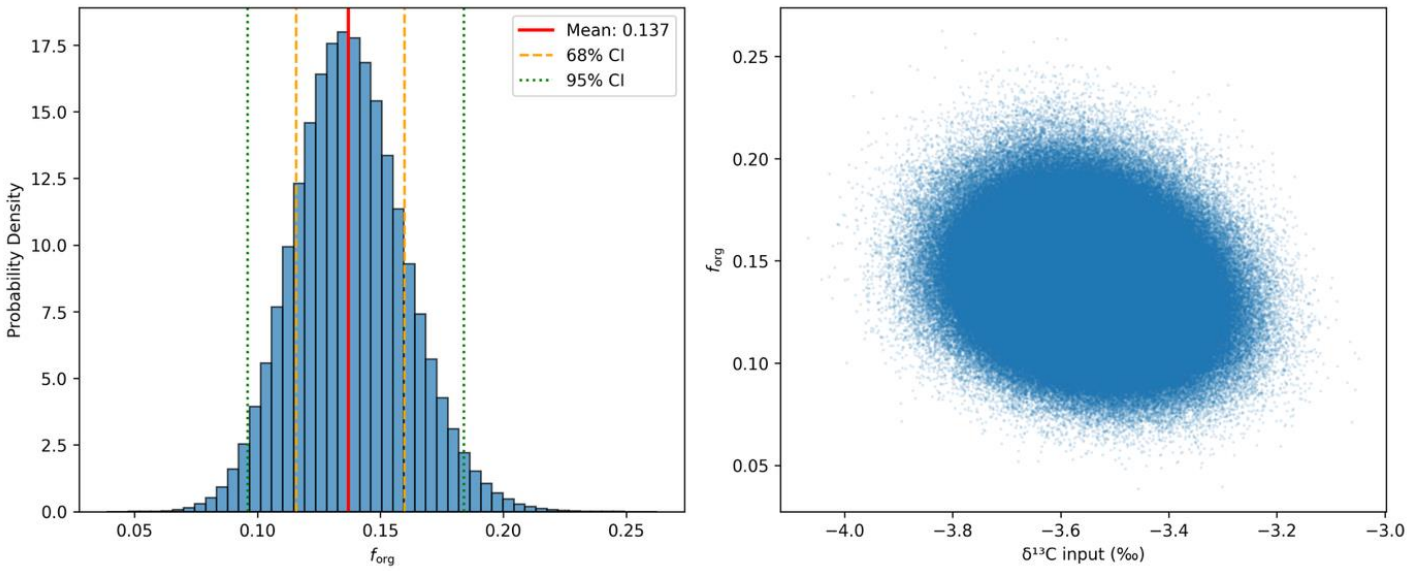

Figure S-6 Monte Carlo analysis of fractional organic carbon burial (f_{org}) using the canonical mantle carbon isotope composition ($\delta^{13}C_{mantle}$ = -4.9 ± 1.9‰; Stachel *et al.*, 2022). (Left) Probability density histogram showing the distribution of f_{org} values with mean = 0.190 (19.0%, red line), 68% confidence intervals (11.5–26.8%, orange dashed lines), and 95% confidence intervals (4.8–34.6%, green dotted lines). (Right) Scatter plot illustrating the inverse relationship between $\delta^{13}C$ input values and calculated f_{org}, with point density reflecting the underlying parameter distributions. The broad elliptical distribution reflects the large uncertainty associated with the canonical mantle isotope composition and its propagation through the mass balance calculation. The results demonstrate that use of the canonical mantle endmember yields $f_{org} = 19.0^{+7.8}_{-7.5}$%, substantially increasing both the inferred mean and uncertainty relative to calculations using the revised mantle constraint, and extending into ranges inconsistent with independent sedimentary carbon inventory estimates (10–17%), but consistent with the higher isotopic mass-balance estimates of 19-34% reported by Derry (2014).

Supplementary Information References

Derry, L.A. (2014) 12.9 - Organic Carbon Cycling and the Lithosphere. In: Holland, H.D., Turekian, K.K. (Eds.) *Treatise on Geochemistry*. Second Edition, Elsevier, Amsterdam, 239–249. https://doi.org/10.1016/B978-0-08-095975-7.01014-7

Giuliani, A., Dalton, H., Pearson, D.G. (2025) Kimberlites: The deepest geochemical probes of Earth. In: Anbar, A., Weis, D. (Eds.) *Treatise on Geochemistry*. Third Edition, Volume 1, Elsevier, Amsterdam, 159–230. https://doi.org/10.1016/B978-0-323-99762-1.00064-4

Griffin, W.L., Powell, W.J., Pearson, N.J., O'Reilly, S.Y. (2008) Appendix A2: GLITTER: data reduction software for laser ablation ICP-MS. In: Sylvester, P. (Ed.) *Laser Ablation-ICP-MS in the Earth Sciences: Current Practices and Outstanding Issues.* Mineralogical Association of Canada Short Course 40, Vancouver, 308–311. https://doi.org/10.3749/9780921294801.app02

Harris, C.R., Millman, K.J., van der Walt, S.J., Gommers, R., Virtanen, P., Cournapeau, D., Wieser, E., Taylor, J., Berg, S., Smith, N.J., Kern, R., Picus, M., Hoyer, S., van Kerkwijk, M.H., Brett, M., Haldane, A., del Río, J.F., Wiebe, M., Peterson, P., Gérard-Marchant, P., Sheppard, K., Reddy, T., Weckesser, W., Abbasi, H., Gohlke, C., Oliphant, T.E. (2020) Array programming with NumPy. *Nature* 585, 357–362. https://doi.org/10.1038/s41586-020-2649-2

Hauri, E.H., Maclennan, J., McKenzie, D., Gronvold, K., Oskarsson, N., Shimizu, N. (2018) CO_2 content beneath northern Iceland and the variability of mantle carbon. *Geology* 46, 55–58. https://doi.org/10.1130/G39413.1

Hirschmann, M.M. (2018) Comparative deep Earth volatile cycles: The case for C recycling from exosphere/mantle fractionation of major (H_2O, C, N) volatiles and from H_2O/Ce, CO_2/Ba, and CO_2/Nb exosphere ratios. *Earth and Planetary Science Letters* 502, 262–273. https://doi.org/10.1016/j.epsl.2018.08.023

Jochum, K.P., Weis, U., Stoll, B., Kuzmin, D., Yang, Q., Raczek, I., Jacob, D.E., Stracke, A., Birbaum, K., Frick, D.A., Günther, D., Enzweiler, J. (2011) Determination of Reference Values for NIST SRM 610–617 Glasses Following ISO Guidelines. *Geostandards and Geoanalytical Research* 35, 397–429. https://doi.org/10.1111/j.1751-908X.2011.00120.x

Kump, L.R., Arthur, M.A. (1999) Interpreting carbon-isotope excursions: carbonates and organic matter. *Chemical Geology* 161, 181–198. https://doi.org/10.1016/S0009-2541(99)00086-8

Le Voyer, M., Kelley, K.A., Cottrell, E., Hauri, E.H. (2017) Heterogeneity in mantle carbon content from CO_2-undersaturated basalts. *Nature Communications* 8, 14062. https://doi.org/10.1038/ncomms14062

Lee, H., Moussallam, Y., Aubaud, C., Iacono-Marziano, G., Hammond, K., Ebel, D. (2024) Carbon isotope fractionation between CO_2 and carbon in silicate melts at high temperature. *Geochimica et Cosmochimica Acta* 380, 208–219. https://doi.org/10.1016/j.gca.2024.07.015

Lyons, L. (1991) *A Practical Guide to Data Analysis for Physical Science Students*. Cambridge University Press, Cambridge. https://doi.org/10.1017/CBO9781139170321

Maclennan, J., McKenzie, D., Grönvold, K., Shimizu, N., Eiler, J.M., Kitchen, N. (2003a) Melt mixing and crystallization under Theistareykir, northeast Iceland. *Geochemistry, Geophysics, Geosystems* 4, 8624. https://doi.org/10.1029/2003GC000558

Maclennan, J., McKenzie, D., Hilton, F., Gronvöld, K., Shimizu, N. (2003b) Geochemical variability in a single flow from northern Iceland. *Journal of Geophysical Research: Solid Earth* 108, 2007. https://doi.org/10.1029/2000JB000142

Miller, W.G.R., Maclennan, J., Shorttle, O., Gaetani, G.A., Le Roux, V., Klein, F. (2019) Estimating the carbon content of the deep mantle with Icelandic melt inclusions. *Earth and Planetary Science Letters* 523, 115699. https://doi.org/10.1016/j.epsl.2019.07.002

Palme, H., O'Neill, H.St.C. (2014) 3.1 - Cosmochemical Estimates of Mantle Composition. In: Holland, H.D., Turekian, K.K. (Eds.) *Treatise on Geochemistry*. Second Edition, Elsevier, Amsterdam, 1–39. https://doi.org/10.1016/B978-0-08-095975-7.00201-1

Pedregosa, F., Varoquaux, G., Gramfort, A., Michel, V., Thirion, B., Grisel, O., Blondel, M., Prettenhofer, P., Weiss, R., Dubourg, V., Vanderplas, J., Passos, A., Cournapeau, D., Brucher, M., Perrot, M., Duchesnay, E. (2011) Scikit-learn: Machine Learning in Python. *The Journal of Machine Learning Research* 12, 2825–2830. http://jmlr.org/papers/v12/pedregosa11a.html

Press, W.H., Teukolsky, S.A., Vetterling, W.T., Flannery, B.P. (2007) *Numerical Recipes: The Art of Scientific Computing*. Third Edition, Cambridge University Press.

Rubin, K.H., Sinton, J.M., Maclennan, J., Hellebrand, E. (2009) Magmatic filtering of mantle compositions at mid-ocean-ridge volcanoes. *Nature Geoscience* 2, 321–328. https://doi.org/10.1038/ngeo504

Rudge, J.F., Maclennan, J., Stracke, A. (2013) The geochemical consequences of mixing melts from a heterogeneous mantle. *Geochimica et Cosmochimica Acta* 114, 112–143. https://doi.org/10.1016/j.gca.2013.03.042

Saal, A.E., Hauri, E.H., Langmuir, C.H., Perfit, M.R. (2002) Vapour undersaturation in primitive mid-ocean-ridge basalt and the volatile content of Earth's upper mantle. *Nature* 419, 451–455. https://doi.org/10.1038/nature01073

Shea, J., Hughes, E., Balzer, R., Bindeman, I., Blundy, J., Brooker, R., Botcharnikov, R., Cartigny, P., EIMF, Gaetani, G., Kilgour, G., Maclennan, J., Monteleone, B., Neave, D.A., Shorttle, O. (2025a) Improved Precision and Reference Materials for Stable Carbon Isotope Measurement in Basaltic Glasses using Secondary Ion Mass Spectrometry. *Geostandards and Geoanalytical Research* 49, 607–627. https://doi.org/10.1111/ggr.12609

Shea, J., Maclennan, J., Edmonds, M., Hughes, E., Hartley, M., Mikhail, S., Perfit, M., Shorttle, O. (2025b) OlivineOverlord/revised_d13C: GPL submission (v1.0.0). *Zenodo*. https://doi.org/10.5281/zenodo.17399056

Stachel, T., Cartigny, P., Chacko, T., Pearson, D.G. (2022) Carbon and Nitrogen in Mantle-Derived Diamonds. *Reviews in Mineralogy and Geochemistry* 88, 809–875. https://doi.org/10.2138/rmg.2022.88.15

Taracsák, Z., Neave, D.A., Beaudry, P., Gunnarsson-Robin, J., Burgess, R., Edmonds, M., Halldórsson, S.A., Longpré, M.-A., Ono, S., Ranta, E., Stefánsson, A., Turchyn, A.V., EIMF, Hartley, M.E. (2021) Instrumental mass fractionation during sulfur isotope analysis by secondary ion mass spectrometry in natural and synthetic glasses. *Chemical Geology* 578, 120318. https://doi.org/10.1016/j.chemgeo.2021.120318

Taylor, J.R. (1997) *An Introduction to Error Analysis: The Study of Uncertainties in Physical Measurements*. Second Edition, University Science Books, Sausalito.

Virtanen, P., Gommers, R., Oliphant, T.E., Haberland, M., Reddy, T., Cournapeau, D., Burovski, E., Peterson, P., Weckesser, W., Bright, J., van der Walt, S.J., Brett, M., Wilson, J., Millman, K.J., Mayorov, N., Nelson, A.R.J., Jones, E., Kern, R., Larson, E., Carey, C.J., Polat, İ., Feng, Y., Moore, E.W., VanderPlas, J., Laxalde, D., Perktold, J., Cimrman, R., Henriksen, I., Quintero, E.A., Harris, C.R., Archibald, A.M., Ribeiro, A.H., Pedregosa, F., van Mulbregt, P., SciPy 1.0 Contributors (2020) SciPy 1.0: fundamental algorithms for scientific computing in Python. *Nature Methods* 17, 261–272. https://doi.org/10.1038/s41592-019-0686-2